School of Engineering Sciences

Piezoelectric tuning of integrated photonic delay circuits

Anton Möller
antonmol@kth.se

Degree Project in Engineering Physics, Second Cycle, 30 Credits

A thesis submitted in fulfilment of the requirements for the degree of

Master of Science (120 credits)

– *and* –

Master of Science in Engineering, Degree program in Engineering Physics (300 credits)

Anton Möller 0000-0001-6393-4618

Supervisor Dr. Ali Elshaari 0000-0002-7004-9665

Examiner Prof. Val Zwiller 0000-0002-5726-1063

KTH Royal Institute of Technology
School of Engineering Sciences
Department of Applied Physics
Division of Quantum Nano Photonics

TRITA-SCI-GRU 2019:326

Typeset in $\LaTeX$
© Anton Möller, September 22, 2019, all rights reserved.
Printed by Universitetsservice US AB, Stockholm 2019.

Abstract

For realising high-quality complex quantum circuits, scalable on-chip realisations are a viable option. Aside from being inherently stabilised and mobile, the on-chip platform provides the means to achieve true scalability by hybrid integration of the three main parts; generation, manipulation and detection.

Delay line elements are crucial parts of any complex quantum circuit as they can be used to do time-domain processing and allow for pulse arrival time synchronising. This thesis therefore present one approach for delaying optical pulses; namely by coupled ring resonators. Specifically, the work focuses on CROWs (serially coupled ring resonators) and their delay characteristics.

Furthermore, the impact of viable on-chip delay devices is limited unless the elements can be tuned. Because of the ambitious usage goals and operating regimes, piezoelectric tuning was chosen as it allows for cryogenic operation, has a low thermal budget and can be implemented in existing device fabrication techniques.

We demonstrate up to 0.30 nm piezoelectric resonance tuning for SiN/SiO_2 devices on PMN-PT carrier wafers for a variety of configurations including all-pass resonators, add-drop resonators and multiple-ring CROWs with simulated theoretical delays in excess of 100 ps and measured experimental intrinsic quality factors around 10000. This resonance tuning range corresponds to a 90 ps group delay tuning range. In addition, we demonstrate high-quality resonator devices on silicon carrier wafers with measured experimental intrinsic quality factors reaching 100000 and experimentally extracted group delays on the order of 30 ps.

Preface

The research that has gone into the writing and completion of this thesis has been truly enjoyable. I have first-hand got to take part in every stage of the research process, from theoretical modelling, prototyping, actual fabrication, taking measurement and performing the data analysis. Because to this, I walk away with much new knowledge and invaluable practical know-how.

Anton Möller
Stockholm, 2019

Acknowledgements

This thesis could not have come together without my excellent supervisor, Dr. Ali Elshaari. With his kind words, dedication, encouragement and learning-by-doing approach, he has continuously challenged me while sparking my interest and keeping me motivated. In lack for better words, I could not have wished for a better supervisor.

Secondly, I would like to thank my examiner, Prof. Val Zwiller, that in addition to opening his research group for me always has been encouraging and provided valuable insight.

Thirdly, I extend my gratitude to PhD candidate Thomas Lettner for having taught and showed me important fabrication techniques, assisting with the electrical control of the piezoelectric samples and never hesitating to taking time answering questions. Furthermore, I would like to thank PhD candidate Samuel Gyger for always providing assistance in everything from optical setup building, to CAD designs and fruitful discussions.

Finally, I would like to thanks all members of the Quantum Nano Photonics group for taking me in during this time, for helping me whenever I needed it and also for pushing the quality of the work that is carried out higher and higher.

Contents

Preliminaries **i**
Abstract i
Preface iii
Acknowledgements iii

1 Introduction **1**
1.1 Background 1
1.2 Photonics and integrated circuits 2
1.3 Dynamical tuning of optical elements 3
1.4 Piezoelectric tuning 5
1.5 Delay of optical signals 8
1.6 Aim and objectives 11
1.7 Outline of the thesis 12

2 Waveguide physics and numerical simulations **15**
2.1 Propagation of light in dielectric media 15
2.2 Resonant photonic cavities 16
2.2.1 All-pass ring resonators 17
2.2.2 Add-drop ring resonators 21
2.2.3 Coupled ring resonators 24
2.3 Numerical simulations 29
2.3.1 Coupling strengths 29
2.3.2 Time domain models of CROWs 32

3 Fabrication and characterisation **35**
3.1 Technology of nanofabrication 35
3.1.1 Lithography 35

3.1.2 Etching 37
3.1.3 Plasma enhanced chemical vapor deposition . . 40
3.1.4 Electron-beam physical vapor deposition 40
3.2 On-chip device fabrication 41
3.3 Piezoelectric device fabrication 47
3.4 Sample cleaving and mounting 52
3.5 Room temperature chip characterisation 54
3.5.1 Transmission spectroscopy 54

4 Results and analysis 57
4.1 Silicon substrates 57
4.2 PMN-PT substrate 60

5 Discussion 69
5.1 Silicon prototype devices 70
5.2 PMN-PT tunable devices 71
5.3 Future work 72

References 75

A Sample mounting 85

B Measurement mounting 87

C Raw transmission spectroscopy spectra 89

D Numerical models 93

List of Figures

1.1 Principal lattice strains 6
1.2 Anomalous dispersion curve 10
1.3 3-ring CROW schematic 12

2.1 Schematic of an all-pass resonator 17
2.2 All-pass resonator spectral response 20
2.3 All-pass resonator group delay 20
2.4 Schematic of an add-drop resonator 22
2.5 Add-drop resonator spectral response 23
2.6 Add-drop resonator group delay 23
2.7 General CROW schematic 25
2.8 4-ring CROW spectral response 28
2.9 4-ring CROW group delay 28
2.10 Numerical simulation region 29
2.11 Schematic of the resonator-bus coupling region 30
2.12 Power coupling coefficients for straight bus 31
2.13 Power coupling coefficients for bent bus 31
2.14 Time domain simulation for a 9-ring CROW 34

3.1 Positive and negative resist development 36
3.2 Electron-beam lithography schematic 36
3.3 Etching selectivity and isotropy 38
3.4 ICP-RIE etching schematic 39
3.5 Electron-beam PVD system schematic 41
3.6 Step-by-step fabrication process illustration 43
3.7 Piezoelectric substrate poling illustration 48
3.8 Ring resonator SEM images 1/2 49

3.8 Ring resonator SEM images 2/2 50
3.9 Sidewall SEM images 51
3.10 Sample mounting overview 53
3.11 Experimental setup 56

4.1 All-pass silicon substrate cavity parameters 58
4.2 Add-drop silicon substrate cavity resonances 59
4.3 CROW drop port resonances 60
4.4 All-pass TE and TM spectra for 200 nm coupling gap . 62
4.5 All-pass TE and TM spectra for 250 nm coupling gap . 62
4.6 Q-value and extinction ratio spatial trends 63
4.7 CROW drop port TE and TM spectra 64
4.8 CROW through port TE and TM spectra 64
4.9 IV poling curve 65
4.10 All-pass resonator piezoelectric tuning shifts 67
4.11 CROW piezoelectric tuning shifts 67
4.12 All-pass piezoelectric tuning spectra 68
4.13 CROW drop port piezoelectric tuning spectra 68

5.1 Quantum emitters correlation measurement 73

A.1 Sample mounting overview 85
A.2 Schematic of the sample mounting process 86

B.1 Mount and external contacting 87
B.2 Measurement sample mounting 88

C.1 Raw all-pass TE and TM spectra for 200 nm coupling gap 90
C.2 Raw all-pass TE and TM spectra for 250 nm coupling gap 90
C.3 Raw CROW drop port TE and TM spectra 91
C.4 Raw CROW through port TE and TM spectra 91

1 Introduction

1.1 Background

Quantum science and photons have long been strongly associated notions [1]. With the concept of single photons proposed over 100 years ago [2], single photon sources emerging in the late 70s by isolated atomic transitions [3–5], and the recent introduction of alternate single photon sources (such as material defect centres [6–8] and quantum dots [9, 10]), single photon manipulation and detection is now the starting point for novel photonic technologies where the goal is to realise scalable quantum optical circuits which require on-chip single photon generation, manipulation and detection.

Harnessing the photon as an information carrier has proven resourceful, much owing to the many possible encoding schemes available. Information could for example be encoded onto the photon by polarisation [11, 12], spatially [13, 14], in frequency domain [15, 16], in time domain [17–19] or even by combinations of these [20–22] which make photons a versatile choice for carriers.

Using photons as quantum bits (qubits) is a natural choice for long-distance quantum communication and linear optical quantum computing (LOQC) implementations. Should such schemes be realised, the attainable technologies would range from unbreakable quantum encryption schemes facilitating everything from secure bank transfers to large-scale secure networks [1, 23]. Furthermore, certain tasks with high complexity for the current electronic computing technologies, such as factoring large numbers and manipulating large matrices, would see a significant reduction in their complexity using quantum computing technology [24–26].

1.2 Photonics and integrated circuits

The main problem with off-chip implementations of LOQC are the bulky components. These not only require specialised laboration setups, but are also inherently immobile, unnecessarily complex and must be externally stabilised to function optimally [23, 27]. On the contrary, integrated on-chip nanophotonic devices are mobile, inherently stabilised and requires little to no permanent infrastructure as every component from source to detection can be fixed in relation to each other. Furthermore, the on-chip platform provides the means to achieve implementable scalability, which has been one of the main hurdles to overcome with table-top LOQC realisations [27–29].

Every implementation of a LOQC scheme requires three fundamental parts. Firstly, the information carrier generation, i.e. single photon generation; secondly, the manipulation of these carriers in some way, for example filtering, routing and/or switching; and thirdly, the information read-out of the carriers, i.e. the detection of the photons [23, 27].

As discussed, information can be encoded onto single photons in many ways, but before encoding anything, the photons must be generated by some process. To utilise the system's quantum properties, the generation process of photons should efficiently emit single photons (and have small probability for multi-photon emissions), preferably emit with directionality and have high photon indistinguishability. A promising generation candidate are (III-V) quantum dots (QDs) that in addition to near ideal single photon emission [30, 31] have potential for on-demand light generation [32], photonic circuit integration [28, 29] and integration to other nanocavities [9, 33, 34].

For carrier manipulation, the photonic platform stands out as a suitable candidate as every discrete unitary operator can be constructed from the fundamental optical components beam splitters and mirrors [35], and complex manipulation schemes have already been demonstrated [36, 37]. Furthermore, silicon-based circuits have potential for low propagation losses and high quality circuits, which are necessary for the delicate nature of single photon processing, owing to the very developed nanofabrication technology adapted from the microelectronics industry for the silicon platform compared to the III-V

platform [38–40].

Finally, the detection (read-out) process should be highly efficient for single photon detection, present low timing jitter and in addition present a low dark count rate. Superconducting nanowire single photon detectors (SNSPDs) are currently the state-of-art single photon detection technology that addresses these issues [41] and furthermore have been successfully implemented in silicon-based circuits [34].

With that said, we turn to the main problem of efficient LOQC implementations: Successful realisations of miniaturised, scalable on-chip quantum computing schemes require the carrier generation, the carrier manipulation and the carrier detection processes all to be brought together and combined. This sounds straightforward but is in practice a great challenge due to the incompatibility of certain technologies. Much effort has been put into developing hybrid approaches [28, 29, 42], by for example integrating QD in nanowires that then are deposited as an on-chip single photon source [43] and integrating SNSPDs in photonic circuits [43, 44], but there are still challenges to overcome.

1.3 Dynamical tuning of optical elements

A single purpose on-chip implementation can thus be realised if these components can be brought together. For more complex purposes, non-tunable chips will generally not suffice, which leads to the concept of dynamical tuning of optical elements.

The main way to achieve dynamical tuning on chip (i.e. dynamically change the physical properties of the optical elements in a way that alter system properties, such as the operating wavelength, acceptance bandwidth et cetera), is by causing the carrier material to change its refractive index $n \to n + \Delta n$ [45].

There are several ways of tuning optical elements and some of the main techniques will now be presented.

Electro-optic effect

The electro-optical effect entails that the refractive index of a material changes in response to an externally applied electrical field. This

change Δn can be proportional to the applied field (called Pockels effect, $\Delta n \propto \mathbf{E}$), or to higher powers of the field (e.g. Kerr effect for $\Delta n \propto \mathbf{E}^2$).

The perturbation of the refractive index also depends on the electro-optical coefficients of the material in question [46], and in particular, the Pockels effect only applies to crystals with lattice structures that lack inversion symmetry or other materials that are non-centrosymmetric (i.e. it is a second order nonlinear effect), such as lithium niobate [47].

For centrosymmetric lattices (such as silicon nitride) this leaves the (generally) orders of magnitude weaker Kerr effect that is present in all materials (it is a third order nonlinear effect) [48, 49].

For a fully integrated on chip computing scheme, the Kerr effect has not yet been utilised as a modulation technique, owing to the relative tuning weakness and the availability of other techniques.

Thermo-optical effect

Material properties are heavily dependent on the crystal lattice structure and the lattice parameters (i.e. the physical separation distance between atoms) which in conjunction with the band gap structure contribute to the electrical properties such as the refractive index [50].

Thermo-optic effects in materials are well-known and can be utilised for circuit tuning by cooling or heating. The addition or removal of heat does not cause the refractive index to change directly, but rather through the photon-phonon interactions, the strength of which can be controlled by adding or removing heat. However, the thermo-optical effect is not to be confused with thermal expansion, which physically stretches or shrinks the sample in response to heat, thereby inducing refractive index shifts [51]. However, both effects do contribute to the thermal tuning of the refractive index, but the former is generally larger, and the latter therefore neglected.

Recently, much focus has been put into more effective circuits, which has led to the introduction of cryogenic operating temperatures and for example state-of-art SNSPDs operate on the superconductivity principle [41]. This operating temperature clearly opposes the whole concept of thermal tuning and is therefore not a suitable tuning method for future-proof technologies.

Free carrier plasma dispersion effect

Another common way of changing the physical properties of materials is through injection of free electrons or holes, jointly referred to as carriers, into the material. This causes the effective band structure of the device to change which implies injection or depletion of carriers into the region where the optical mode resides, and thereby changing the effective refractive index. This can be realised in several ways, most commonly through p-i-n diodes over which a tunable voltage is applied [52–54].

This allows for precise dynamical tuning in materials with relatively small band gaps (such as semiconductors and doped materials). However, a large class of materials are insulating with distinct valence and conduction bands, including silicon nitride, which render this effect unusable. Furthermore, the free carrier dispersion effect requires some method of creating p-i-n junctions, which is not trivial in most cases [50].

1.4 Piezoelectric tuning

Piezoelectric tuning is alternative method of tuning that works for any type of circuit material, insulators included, and in addition have very low thermal budget (i.e. work in cryogenic operating conditions). A material that is piezoelectric will change its electric polarisation in response to an applied strain, and similarly by applying an electric field, stresses and strain will be induced in a piezoelectric material [50]. By fabricating the desired photonic circuit on top of such a material, the strain transfer between the piezoelectric carrier wafer and circuit stack induces the desired tuning.

Historically, this scheme has successfully been used to precisely tune the emission wavelengths of quantum dots [55–57] as well as tuning integrated optical emitters on chip [28, 29] and also to reconfigure optical elements on chip [29, 58].

Piezoelectric properties are found in non-centrosymmetric materials (i.e. materials without inversion symmetry). Such materials lack lattice symmetry which causes spontaneous polarisation domains to occur in the crystal lattice. Domains polarised in the same directions

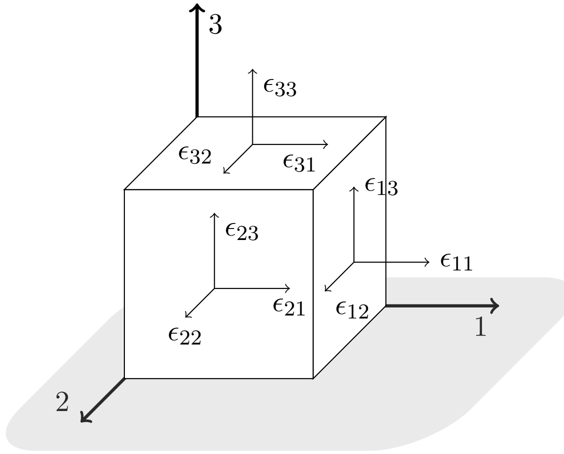

Figure 1.1: *Principal lattice direction* 1, 2 *and* 3 *with corresponding components* ϵ_{ij} *of the strain tensor* $\boldsymbol{\epsilon}$ *for an arbitrary material.*

form piezoelectric domains and the global interplay between many piezoelectric domains give the observed material properties [59].

As previously discussed, changes in the electro-optical properties of a material are influenced by for example lattice constants and lattice structure, and the strain changes occurring the in a piezoelectric crystal lattice as a result of external electric fields therefore give rise to changes in the electro-optical properties that can be dynamically and reversible controlled by tuning the applied field.

Strain and stresses

Conceptually, strain can be thought of as deformation resulting from an applied stress which is nothing other than a force applied on a surface.

The strain of a material is described using the strain tensor $\bar{\boldsymbol{\epsilon}}$ with components

$$\epsilon_{ij}, \quad i, j \in \ \{1, 2, 3\}$$

along the principal material axes $1, 2, 3$ as shown in figure 1.1. Components with symmetric indices $(i = j)$ describe strains along the principal axes acting on planes normal to those directions. Mixed index components on the other hand $(i \neq j)$ describe out-of-plane

strains, that is, strains on planes parallel to the direction of the applied stresses. Due to symmetries the full 3×3 strain matrix is often simplified to the 6×1 strain vector $\boldsymbol{\epsilon} = [\epsilon_{11}, \epsilon_{22}, \epsilon_{33}, \epsilon_{23}, \epsilon_{31}, \epsilon_{12}]^T$ using so called Voigt notation [50].

Given a piezoelectric material with piezoelectric strain tensor $\bar{\bar{d}}$ and elastic compliance tensor (inverse of the elasticity tensor) $\bar{\bar{s}}$ subject to the external stress $\boldsymbol{\sigma}$ and external electric field $\mathbf{E}$, the resulting strain is given by

$$\boldsymbol{\epsilon} = \bar{\bar{s}} \cdot \boldsymbol{\sigma} + \bar{\bar{d}} \cdot \mathbf{E}, \tag{1.1}$$

or on component form

$$\begin{bmatrix} \epsilon_{11} \\ \epsilon_{22} \\ \epsilon_{33} \\ \epsilon_{23} \\ \epsilon_{31} \\ \epsilon_{12} \end{bmatrix} = \begin{bmatrix} s_{11} & \cdots & s_{16} \\ s_{21} & \cdots & s_{26} \\ s_{31} & \cdots & s_{36} \\ s_{41} & \cdots & s_{46} \\ s_{51} & \cdots & s_{56} \\ s_{61} & \cdots & s_{66} \end{bmatrix} \cdot \begin{bmatrix} \sigma_{11} \\ \sigma_{22} \\ \sigma_{33} \\ \sigma_{23} \\ \sigma_{31} \\ \sigma_{12} \end{bmatrix} + \begin{bmatrix} d_{11} & d_{12} & d_{13} \\ d_{21} & d_{22} & d_{23} \\ d_{31} & d_{32} & d_{33} \\ d_{41} & d_{42} & d_{43} \\ d_{51} & d_{52} & d_{53} \\ d_{61} & d_{62} & d_{63} \end{bmatrix} \cdot \begin{bmatrix} E_1 \\ E_2 \\ E_3 \end{bmatrix} \tag{1.2}$$

When using piezoelectricity for optical tuning, the external stress $\boldsymbol{\sigma}$ is usually zero which yield a linear relation between the strain $\boldsymbol{\epsilon}$ and applied electrical field $\mathbf{E}$ where the piezoelectric strain tensor $\bar{\bar{d}}$ serving as the proportionality constant. Furthermore, the piezoelectric strain tensor is often highly symmetric and has many elements with relations between them owing to crystal symmetries. Consider for example the crystal PMN-PT which is the piezoelectric substrate material used in this thesis. The non-zero, independent piezoelectric strain tensor elements for PMN-PT are

$$\begin{aligned} d_{13} = d_{23} &= -699\,\mathrm{pC/N} \\ d_{33} &= 1540\,\mathrm{pC/N} \\ d_{42} = d_{51} &= 164\,\mathrm{pC/N} \end{aligned}$$

which greatly simplifies the analysis [59, 60].

In addition, for an applied electric field only in the third principal direction $\left(\mathbf{E} = [0,\ 0,\ E_3]^T\right)$ the mixed-index components of the strain tensor are zero leaving only strains along the principal axes,

$$\begin{aligned} \epsilon_{11} = \epsilon_{22} &= d_{13} E_3 \\ \epsilon_{33} &= d_{33} E_3 \end{aligned}$$

which is (as we shall see) one of the reasons PMN-PT was chosen as the piezoelectric substrate in this thesis.

PMN-PT

The solid solution of lead magnesium niobate (PMN) and lead titanate (PT), commonly abbreviated PMN-PT, is a relaxor ferroelectric material with a perovskite lattice structure. It is a highly piezoelectric material composed by

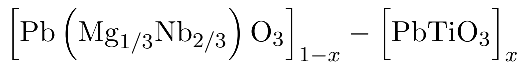

$$\left[\mathrm{Pb}\left(\mathrm{Mg}_{1/3}\mathrm{Nb}_{2/3}\right)\mathrm{O}_3\right]_{1-x} - \left[\mathrm{PbTiO}_3\right]_x$$

where the fraction x determine the mix between the two main components. It has been shown that for mixes around $x \approx 0.3$ the material undergoes a morphotropic phase transition between a rhombohedral and a tetragonal structure giving rise to the most favourable piezoelectric properties. The actual mixing fractions for manufacturing chips are finely tuned around 30% such that the best piezoelectric properties are obtained while still maintaining structural integrity and stability [61–63].

As a piezoelectric actuator, PMN-PT offers the ability to engineer phase transition boundaries and domains [63] and provides almost an order of magnitude larger piezoelectric coefficients [64, 65] with ultra-high strain levels approaching 2% in comparison to other substrates.

Furthermore, PMN-PT allows for cryogenic circuit integration which is highly favourable when working with embedded quantum circuits at low temperatures [66], which makes it the substrate of choice for this thesis.

1.5 Delay of optical signals

Optical signals propagating through media can be thought of as either propagating waves or particles. While neither picture is fully correct, they both provide some insight. Generally, there are two velocities of interest for propagating light. Firstly, there is the phase velocity, i.e. the velocity that the phase of the light travels with. It is the commonly referred to velocity of light pulses and is dictated by the

refractive index n of the material as

$$v_p = \frac{c}{n} = \frac{\omega}{k},$$

where c is the speed of light in vacuum, ω is the angular frequency of the wave and k is the wave number. Conceptually, the phase velocity is the velocity that any given phase of the pulse (for example a crest or a trough) will propagate at [67, Ch. 7].

Group velocity on the other hand is the velocity that the signal envelope propagates with. It is dictated by the frequency dispersion relation $\omega(k)$ and given by

$$v_g = \frac{\partial \omega}{\partial k} = \frac{c}{n - \lambda_0 \frac{\partial n}{\partial \lambda_0}} = v_p - \lambda \frac{\partial v_p}{\partial \lambda},$$

for the vacuum wavelength λ_0 and medium wavelength λ. Information is encoded onto sinusoidal waves by either amplitude, frequency modulation or combination of both. Either way, the velocity at which encoded information is transmitted is the group velocity[1] of the wave packets [67, Ch. 7]

The take-away from this is that the group velocity dictates the information flow rate, and that by careful design one can control this velocity. Especially notice that a large group velocity corresponds to a (magnitude-wise) large derivative of the dispersion relation $\omega(k)$ which is indicative of a rapid-changing refractive index in specific regions. Slowing down propagating light pulse envelopes by modulation of the group velocity effectively serves as a delay of the final arrival time of the pulse which has many useful applications.

For integrated circuits and LOQC, the concept of delay on chip addresses the issue of temporarily storing pulses and retrieving them on demand and furthermore enables time-domain processing in the form of multiplexing and retiming [69, 70]. Furthermore, the impact

[1] In reality information is transmitted by the signal velocity, that with a few exceptions is equal to the group velocity. Exceptions include for example cases where the pulse shape is heavily skewed as a result of asymmetric heavy amplification causing the group velocity to exceed the speed of light thereby violating causality if the information is transmitted thereby. However, in all cases the signal velocity is less than the speed of light, and for our purposes is equal to the group velocity [68].

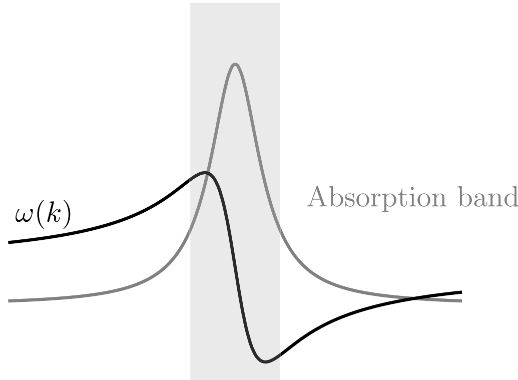

Figure 1.2: *Typical dispersion curve in the vicinity of an absorption band highlighting the anomalous dispersion behaviour that occurs near system resonances.*

of delaying signals on chip cannot be understated. With applications ranging from synchronising arrival times and phase shifts for different beam paths, acting as optical buffers being a fundamental building block in quantum circuits, a tunable optical delay on chip is an integral part of any scalable, reliable and multi-purpose integrated quantum circuit.

Traditionally, delay of pulses was realised using media where one designed the absorption band to hold a strong atomic resonance. Near such a resonance, the dispersion function $\omega(k)$ rapidly changes (shown in figure 1.2) which as discussed introduces a large shift in the group velocity [67, 70, 71]. By inducing transparency in otherwise opaque media using quantum methods like electromagnetically induced transparency (EIT), larger delays (smaller v_g) have been demonstrated [72]. In 1999, researchers reported light propagating in as little as 17 m/s in ultracold atoms using EIT [73] and in the following years completely stopped light [74, 75] and dynamical delay control [76–78] was reported.

Following these realisations, the focus turned to photonic structures to address some of the challenges. For inducing rapid dispersion changes which in turn are associated with delaying the light pulses, one can either utilise photonic crystal structures which are multidi-

mensional structures with periodically introduced small defects that induce dispersion [70] or generate the rapid changes in dispersion through constructive and destructive interference of different optical paths [79], the latter of which is the chosen method in this thesis.

The advantages of these structures are that they are small-scale and, as discussed previously, this is one of the main requirements for scalable integrated devices. Furthermore, these types of structures provide the means to easily design and manipulate the behaviour with the various types of optical tuning that has been discussed [80, 81].

An alternative approach for realising delays is by using microelectromechanical systems (MEMS) whereby circuit reconfiguration (i.e. tunability) can be achieved by mechanical actuation. This is a viable, but inherently unscalable approach. The MEMS industry benefits from very well-developed and precise fabrication techniques, but the mechanical actuation require that the circuit is suspended in a frame, which is a fatal flaw hindering scalability [82–84].

1.6 Aim and objectives

As discussed, there are several challenges for successful implementation of LOQC schemes, two of which being scalability and intra-component compatibility. This thesis aims to address one very specific on-chip component, namely, to realise a scalable and piezoelectrically tunable on-chip optical delay circuit. By working on chip, we have the potential for scalable and portable devices. Furthermore, the highly developed fabrication technologies for silicon-based chips makes the silicon-silicon nitride platform an excellent choice. In addition, the piezoelectrical tuning mechanisms are compatible with our integrated scalable scheme and platform choice while still offering the desired tuning properties and the optical delay.

Specifically, we wish to achieve this tunable delay by using a photonic structure called a CROW, that is a coupled resonator optical waveguide structure whose theory we will expand on in the following chapters. Briefly, it is a series of coupled ring resonators, i.e. circular waveguides positioned in the vicinity of each other as depicted in figure 1.3. Ring resonators are commonly used as wavelength fil-

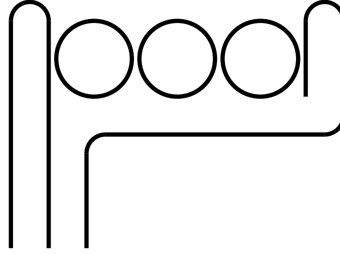

Figure 1.3: *Molecule type ring resonator CROW with $N = 3$ rings and connecting waveguides (through port, in port and drop port from left to right).*

ters as they allow only travelling wave resonant frequencies to pass through, but they have in addition proven useful for delay of optical signals by containing the circulating resonant light with low losses for some time, limited by the time-bandwidth product of the system [85–88]. By combining and stacking these effects in serially coupled rings previously done without piezoelectric tuning, we aim to achieve the discussed on-chip tunable delay. We will expand on the fundamental theory of these structures in the following chapters.

1.7 Outline of the thesis

The outline of the thesis is the following.

In Chapter 2, the theory governing waveguide propagation will be briefly expanded on. The theory will then be applied to resonant cavities, with focus on ring resonators, whose theory and analytic treatment will be presented starting with all-pass devices, followed by add-drop devices and then finally the CROW devices. After that, a time domain simulation technique applicable for any resonator configuration will be presented.

In Chapter 3, the fundamental elements and techniques of nanofabrication will first be presented. Then, the specific fabrication steps used in this thesis are laid out for both silicon and piezoelectric substrates. Furthermore, the fabrication post-processing steps of cleaving and mounting prior to measurements are also detailed, followed by the measurement procedure and setup.

In Chapter 4, the analysed data and results from measurements are presented for both the prototyping on silicon substrates as well as the tunable piezoelectric substrates for an excerpt of the devices fabricated.

Finally, in Chapter 5 the results are discussed and contextualised and the future direction and possible future works of the research is discussed.

Following the body, Appendices A and B detail the piezoelectric mounting and actuation, Appendix C show raw spectra (that in the thesis body are flattened) from transmission spectroscopy measurements and Appendix D contain example code snippets implementing the numerical methods described in Chapter 2.

2 Waveguide physics and numerical simulations

In this chapter, the theory of light propagation is first expanded on, followed by specific examples. For these resonant cavities, the basic theoretical analysis is carried out with a numerical method simultaneously presented. Finally, time-domain simulation tools are presented for full wave propagation as well as FDTD methods for analysing the coupling strength between cavities and bus waveguides.

2.1 Propagation of light in dielectric media

In this section, the basics of light propagation in confined dielectric media is presented. All propagation of light in any media is governed by Maxwell's equations with the proper boundary conditions along the dielectric boundaries. These are complicated to work with and thus require some explanation and simplification.

Light confined in any cavity will oscillate in different *modes*, the form of which depend on the geometry in question. These modes are the travelling wave generalisation of simple resonances within the cavity.

Backing up briefly, the basis of all wave propagation in dielectric media is the wave equation (which is derived from Maxwell's equations under some simplifications). The wave equation for the electrical field $\mathbf{E}$ is usually written as (in the time domain but can also be written in the frequency domain if convenient)

$$\nabla^2\mathbf{E}(\mathbf{r}) + k_0^2 n(\mathbf{r})^2\mathbf{E}(\mathbf{r}) = 0 \tag{2.1}$$

where $n(\mathbf{r})$ is the spatially varying refractive index and $k_0 = 2\pi/\lambda$ is the vacuum propagation constant at the wavelength λ.

Imposing the appropriate boundary conditions and initial conditions, that is, imposing the continuity of the tangential field components over the dielectric boundaries, yield an eigenproblem. Waveguides are often isotropic in one or more direction(s) and confines light in the other(s), and this can be exploited by taking the time evolution of the electrical field to be as exponential along the main (isotropic) propagation direction(s) z,

$$\mathbf{E}(\mathbf{r}, t) = \mathbf{E} \exp i(\omega t \pm \beta z), \tag{2.2}$$

greatly simplifying the analytic problem. Here, ω is the frequency of the propagating light, $\beta = k_0 n = \beta(\omega)$ is the mode specific propagation constant and $\mathbf{E}$ is the cross-sectional electric field distribution that the eigenproblem now concern.

The confinement of light quantifies the eigenproblem which gives a discrete set $m = 1, 2, 3, \ldots$ of field distributions and propagation constant solution pairs (jointly referred to as modes)

$$(\mathbf{E}_m,\ \beta_m), \tag{2.3}$$

where $\beta_m = k_0 n_{m,\text{eff}}$ is the *effective mode propagation constant* that dictates the effective pulse propagation through the device under consideration. These eigenproblems are usually not solvable analytically (except for a few geometries) and therefore treated numerically, which we will return to in section 2.3.

2.2 Resonant photonic cavities

Many different resonant cavity types exist for the silicon-on-insulator platform, and the ring resonator is one of them. As discussed, one purpose of a resonant cavity is to serve as buffer for light and therefore low losses and high buffer times are desired.

As a design option for buffering time structures, ring resonators have proven useful in many different aspects.

Firstly, ring resonators can be designed to serve single transverse mode and specific polarisation components with control of the free

spectral range (FSR, which is the resonance-resonance separation) as it is inversely proportional to the ring radius. Other resonators, such as disk or micro-toroidal resonators) often support multi-mode operation making them unusable for many applications.

Secondly, being travelling-wave cavities, ring resonators ideally does not introduce back-propagation of light in the circuit, opposed to standing-wave cavities which do. This also allows for add-drop configurations as we shall see later.

Finally, as the ring resonators can be constructed in the same material as the connecting bus waveguides, the refractive index contrast between the cavity and bus is very small (it is not zero due to different effective refractive indices for straight and bent waveguides) making coupling losses significantly lower than for other techniques [89].

2.2.1 All-pass ring resonators

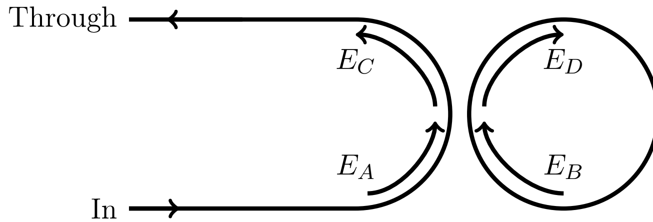

Figure 2.1: *Schematic drawing of an all-pass ring resonator with electrical field quantities marked.*

As depicted in figure 2.1, an all-pass ring resonator consists of a single ring of radius R with one connecting bus waveguide. This bus waveguide has two ports, the in and through ports where the customary notation is that the in port is the port at which the light is coupled in.

The resonant wavelength λ_0 of a ring made of a material with refractive index $n(\lambda)$ is given by

$$2\pi R \cdot n_{\text{eff}}(\lambda_0) = m\lambda_0, \quad m = 1, 2, 3, \ldots \tag{2.4}$$

where $n_{\text{eff}}(\lambda)$ is the effective refractive index at the wavelength λ. Physically, these resonances correspond to a phase difference of 0

(or equivalent a multiple of 2π) and represent the constructive self-interference of the resonant waves.

Generally, the effective refractive index depends on the wavelength of the incident light (dispersion), which give rise to the *effective group refractive index*, $n_{g,\text{eff}}$ defined as

$$n_{g,\text{eff}}(\lambda) = n_{\text{eff}}(\lambda) - \lambda \frac{\mathrm{d}n_{\text{eff}}(\lambda)}{\mathrm{d}\lambda}. \tag{2.5}$$

An important measure is the distance (in wavelength) between adjacent resonances, which is called the free spectral range (FSR). For a ring resonator, the FSR is given by (to a first order approximation of the dispersion)

$$\text{FSR} = \frac{\lambda^2}{n_{g,\text{eff}} L}, \tag{2.6}$$

where $L = 2\pi R$ is the round-trip length of the resonator.

Together with the sharpness of the resonances, the *full width at half maximum* (FWHM) of the Lorentzian resonance lineshape, they form the two fundamental characteristics of the resonances. For determining the overall quality of the cavities, the Q-value Q and finesse $\mathcal{F}$ are used,

$$Q = \frac{\lambda_0}{\text{FWHM}} \tag{2.7}$$

$$\mathcal{F} = \frac{\text{FSR}}{\text{FWHM}}, \tag{2.8}$$

which are dimensionless measures of the resonance width relative its central frequency and the resonance sharpness relative their separation respectively. These values are related to the rate of energy dissipation to internal cavity losses and the bus waveguide(s).

Physically, the Q-value is a measure of the number of field oscillations a light pulse makes in the cavity until $1/e$ of the initial energy remains and similarly the finesse is a measure of how many round-trips the light makes in the cavity before reaching the same energy threshold.

The analytic analysis of a structure like this is carried out considering the phase relations and the induced loss between the different

fields $E_{\mathrm{A-D}}$. Firstly, $e^{-\gamma}$ to be the round-trip decay of the field amplitude and κ to be the field coupling strength of the directional coupler. Secondly, the analysis is carried out using normalised quantities, i.e. the power circulating is taken to be $|E|^2$.

Starting off by considering the coupling region, the waveguide-ring coupling field strength being κ implies that the field transmission $\tau = \sqrt{1-\kappa^2}$ and hence for a given time the relations

$$\begin{bmatrix} E_{\mathrm{C}} \\ E_{\mathrm{D}} \end{bmatrix} = \begin{bmatrix} \tau & i\kappa \\ i\kappa & \tau \end{bmatrix} \begin{bmatrix} E_{\mathrm{A}} \\ E_{\mathrm{B}} \end{bmatrix} \tag{2.9}$$

hold. Furthermore, the fields E_{B} and E_{D} are related by a round-trip worth of phase accumulation and induced loss,

$$E_{\mathrm{B}} = E_{\mathrm{D}} \cdot e^{-\gamma + i\phi} \tag{2.10}$$

where the round-trip phase accumulation (as a function of the wavelength) is given by

$$\phi = n_{\mathrm{eff}}(\lambda) \frac{2\pi}{\lambda} L. \tag{2.11}$$

These equations can be solved to give a relation between the input and output fields as

$$E_{\mathrm{C}} = s_{11} E_{\mathrm{A}} = \left[\tau - \frac{\kappa^2 e^{-\gamma+i\phi}}{1 - \tau e^{-\gamma+i\phi}} \right] E_{\mathrm{A}}, \tag{2.12}$$

or expressed as the measurable transmission

$$T = \frac{|E_{\mathrm{C}}|^2}{|E_{\mathrm{A}}|^2} = 1 - \frac{\left(1 - e^{-2\gamma}\right)\left(1 - \tau^2\right)}{\left(1 - \tau e^{-\gamma}\right)^2 + 4\tau^2 e^{-\gamma} \sin^2 \phi/2}, \tag{2.13}$$

which noticeably has a minimum at the resonant wavelength(s) λ_i, $i = 0, 1, 2, \ldots$ where the phase $\phi(\lambda_i) = 0$ as discussed and shown in figure 2.2.

The minimum transmission is obtained at resonance for $\tau = e^{-\gamma}$, which correspond to the power coupling being equal to the power round trip loss, $\kappa^2 = 1 - e^{-2\gamma}$. This is called *critical coupling* and is a common design goal because of the maximum extinction ratio. When the power coupling is larger than the power round trip loss ($\kappa^2 > 1 - e^{-2\gamma}$), the system is *overcoupled* and conversely *undercoupled*

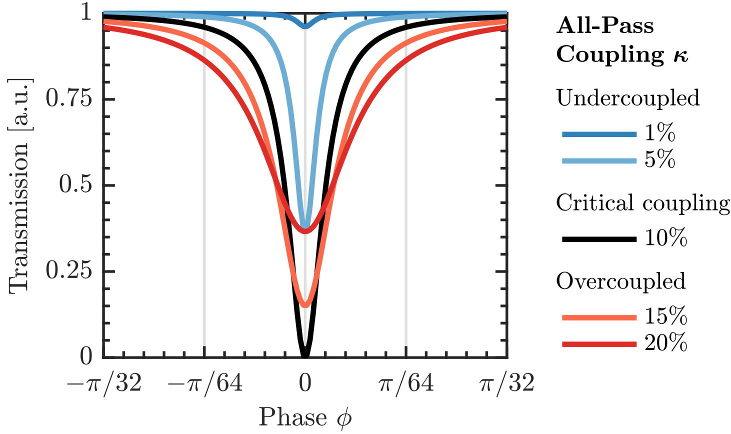

Figure 2.2: *Transmission spectra for an all-pass resonator following eq* (2.13)*. The different lines show different coupling losses for the coupling constant κ in the three coupling regimes (under-, over-, and critical coupling) for a* 1.7 dB/cm *propagation loss, corresponding to a* $\kappa = 10\%$ *critical coupling). Do note the interplay between extinction ratio (peak depth) and lineshape width (FWHM).*

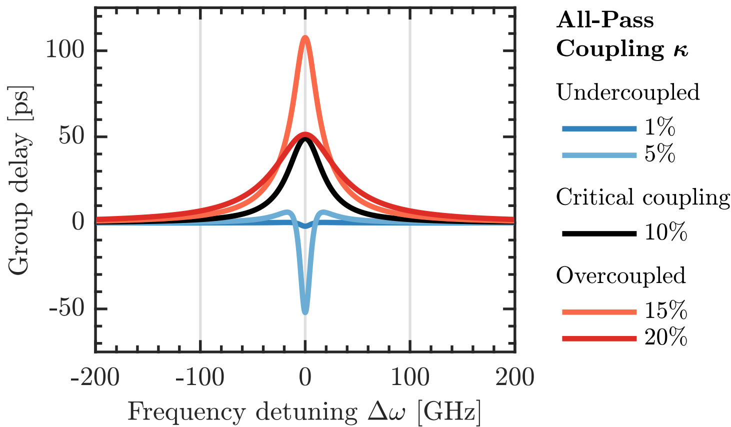

Figure 2.3: *Group delay as a function of frequency detuning (one-to-one correspondence with phase) for* 40 µm *radius ring resonator with the effective index* $n_{\text{eff}} = 1.7$*. Note the corresponding group delay and resonance lineshape extrema in figure 2.2.*

when the loss is larger than the coupling ($\kappa^2 < 1 - e^{-2\gamma}$). The regime of choice depends on the design requirements. There is a fine interplay between extinction ratio and resonance width, both ultimately limited by the coupling factors attainable in the fabrication process.

Another important measure for this type of device is the group refractive index, as discussed. It is related to the maximum delay obtainable and can furthermore be extracted from the transmission function T as the derivative of the complex argument of the proportionality factor s_{11} in eq. (2.12) (as shown in figure 2.3),

$$n_g \propto \frac{\partial \arg s_{11}}{\partial \phi}, \tag{2.14}$$

where the phase ϕ can be related to frequency and wavelength as desired (but this de-generalises the argument as material and geometry specific parameters are introduced) [90]. Do note the correspondence between the Lorentzian lineshape extrema for the resonances in figure 2.2 and the group index in figure 2.3.

For cavities coupled to bus waveguides, one distinguishes between the *intrinsic* and *loaded* quality factors. The intrinsic Q-factor is the factor for the cavity alone, isolated from any external environment, while the loaded quality factor is the one as measured when connected to bus waveguide. Generally, the loaded Q-factor is lower than the intrinsic one as any external bus or environment introduce additional loss thus reducing the Q-factor.

For an all-pass resonator, the intrinsic Q-factor is given by the intrinsic ring loss as

$$Q_i = \frac{\pi n_{g,\text{eff}} L}{\lambda_0 \gamma}, \tag{2.15}$$

while the loaded Q-factor (as given by eq (2.7)) typically is a factor 2 less (although this depends on the relation between the cavity loss and coupling coefficient). Q-factors of $10^5 - 10^6$ are commonly achieved with the current fabrication technology.

2.2.2 Add-drop ring resonators

As shown in figure 2.4, an add-drop configured ring resonator has one additional bus waveguide providing an add and a drop port from

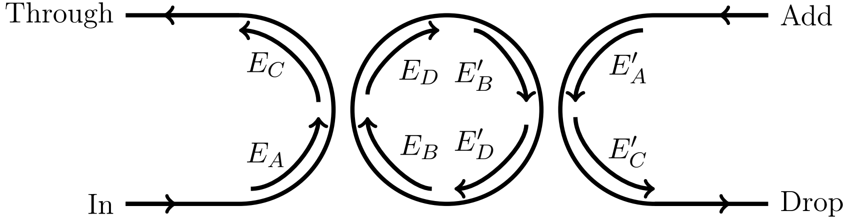

Figure 2.4: *Schematic drawing of an add-drop ring resonator setup.*

which either light can be added or transmission through the ring can be seen. The extra bus waveguide decreases the loaded Q-value of the structure as the extra coupling region apart from serving as an extra source of loss also serves as an escape path for light.

Analytically, the analysis is similar to the all-pass configuration. Each coupling region has a field coupling constant κ_1 and κ_2 that can be different. Associated to the coupling constant, the transmission constants $\tau_{1,2} = \sqrt{1 - \kappa_{1,2}^2}$ are defined in the same manner as before.

Treating each coupling region separately, we get the coupling relations

$$\begin{bmatrix} E_{\text{C}} \\ E_{\text{D}} \end{bmatrix} = \begin{bmatrix} \tau_1 & i\kappa_1 \\ i\kappa_1 & \tau_1 \end{bmatrix} \begin{bmatrix} E_{\text{A}} \\ E_{\text{B}} \end{bmatrix}, \tag{2.16}$$

$$\begin{bmatrix} E'_{\text{C}} \\ E'_{\text{D}} \end{bmatrix} = \begin{bmatrix} \tau_2 & i\kappa_2 \\ i\kappa_2 & \tau_2 \end{bmatrix} \begin{bmatrix} E'_{\text{A}} \\ E'_{\text{B}} \end{bmatrix}, \tag{2.17}$$

and for the intra-ring components the following relations hold

$$E'_{\text{B}} = E_{\text{D}} e^{-\gamma/2 + i\phi/2}, \tag{2.18}$$

$$E_{\text{B}} = E'_{\text{D}} e^{-\gamma/2 + i\phi/2}. \tag{2.19}$$

Once again, these equations can be solved to yield the drop/through port output fields as functions of the input/add port fields on the form

$$\begin{bmatrix} E_{\text{C}} \\ E'_{\text{C}} \end{bmatrix} = \begin{bmatrix} s_{11} & s_{12} \\ s_{21} & s_{22} \end{bmatrix} \begin{bmatrix} E_{\text{A}} \\ E'_{\text{A}} \end{bmatrix}, \tag{2.20}$$

where the matrix is the scattering matrix of the system. By analytic work, the coefficient s_{ij} can be found (and are reported in e.g. [89]).

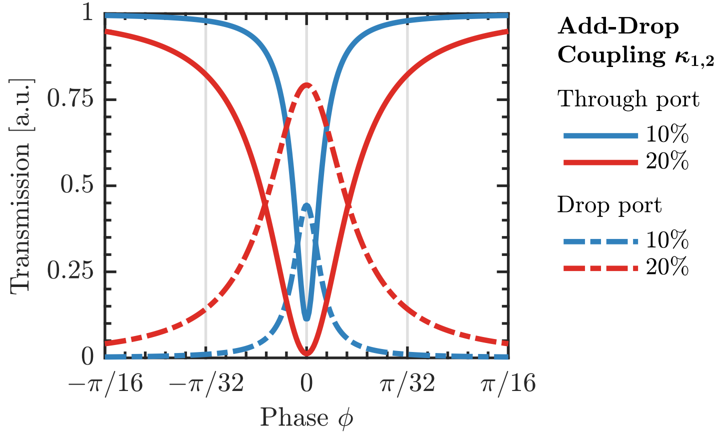

Figure 2.5: *Transmission spectra following eqs.* (2.21) *and* (2.22) *for the through and drop ports of an add-drop resonator respectively. The cases of two different coupling constants are shown (none critically coupled) for a* 1.7 dB/cm *propagation loss.*

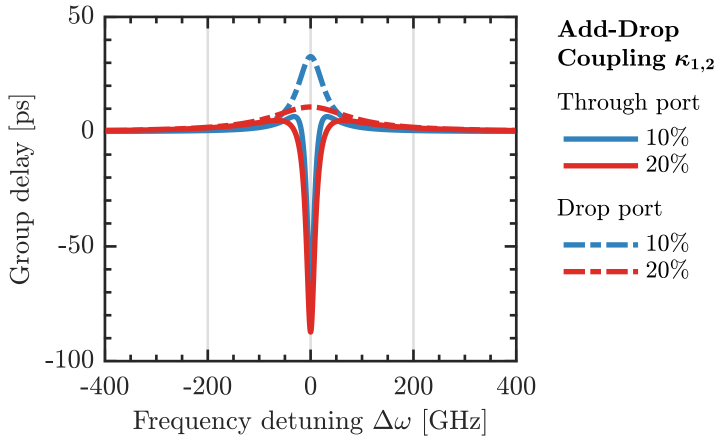

Figure 2.6: *Group delay and advancement as a function of frequency detuning (one-to-one correspondence with phase) for* 40 µm *radius ring resonator with the effective index* $n_{\text{eff}} = 1.7$*. Note the corresponding group delay and resonance lineshape extrema in figure 2.5.*

With no light incident in the add port ($E'_{\mathrm{A}} = 0$), the transmission amplitudes for the through and drop ports are found to be

$$T_{\mathrm{through}} = \frac{|E_{\mathrm{C}}|^2}{|E_{\mathrm{A}}|^2} = |s_{11}|^2 = \frac{(\tau_1 - \tau_2 e^{-\gamma})^2 + 4\tau_1\tau_2 e^{-\gamma}\sin^2\phi/2}{(1-\tau_1\tau_2 e^{-\gamma})^2 + 4\tau_1\tau_2 e^{-\gamma}\sin^2\phi/2} \tag{2.21}$$

$$T_{\mathrm{drop}} = \frac{|E'_{\mathrm{C}}|^2}{|E_{\mathrm{A}}|^2} = |s_{21}|^2 = \frac{e^{-2\gamma}\kappa_1^2\kappa_2^2}{(1-\tau_1\tau_2 e^{-\gamma})^2 + 4\tau_1\tau_2 e^{-\gamma}\sin^2\phi/2} \tag{2.22}$$

which are both characteristic Lorentzian lineshapes, that apart from losses resulting in reduced amplitudes, are complimentary as shown in figure 2.5. In addition, sketches of group delays are shown in figure 2.6, which once again have extrema that correspond nicely with the resonances. The critical coupling condition for an add-drop resonator (minimum transmission at through port on resonance) yield that $\tau_1 = \tau_2 e^{-\gamma}$, which means that the condition cannot be fulfilled for both bus waveguides simultaneously without a negligible loss. Another way of looking at this is that one of the two couplers can always be critically coupled, at the expense of the other coupler regardless of the loss.

Experimentally, the extra bus waveguide introduces an extra source of loss (and hence an extra degree of freedom) compared to the all-pass configuration, which must be accounted for when determining the quality of the cavities. There exist several methods for this, but generally the coupling coefficients $\kappa_{1,2}$ cannot be distinguished from the loss γ unless the coupling strengths are symmetric or the wavelength dependence of the two quantities are employed [91, 92].

2.2.3 Coupled ring resonators

Structures with more than one ring produce more complicated lineshapes (convolutions of the individual single ring lineshape responses) which are desirable in some applications. Generally, cascaded structures give rise to more complex behaviour and are often studied as natural continuations of their simpler predecessors.

For ring resonators, the rings can either be coupled indirectly (similar to a parallel circuit) or directly (i.e. in series). Figure 2.7 shows

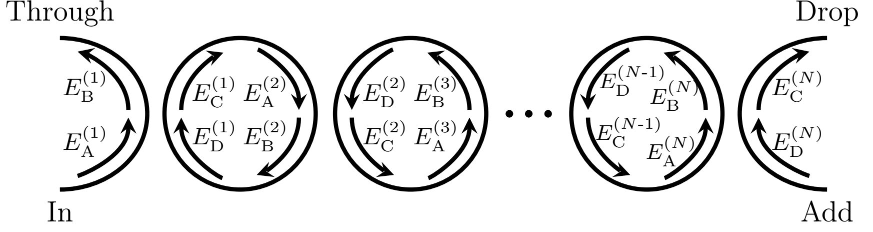

Figure 2.7: *Schematic drawing of a CROW configuration with N coupling regions corresponding to $N-1$ rings.*

a CROW, which contain a number of rings coupled in series to two bus waveguides (i.e. in a generalised add-drop configuration). This configuration can also be thought of as a stacked cascaded wavelength filter structure.

The conceptual analytic analysis follows the same procedure as before. Each coupling region $j = 1, 2, \ldots, N$ has an associated coupling constant κ_j and transmission coefficient $\tau_j = \sqrt{1-\kappa_j^2}$ that relates the fields incident on the coupling region ($E^{(j)}_{\mathrm{A,D}}$) with the outgoing fields ($E^{(j)}_{\mathrm{C,B}}$) as

$$\begin{bmatrix} E_{\mathrm{C}}^{(j)} \\ E_{\mathrm{B}}^{(j)} \end{bmatrix} = \begin{bmatrix} s_{11}^{(j)} & s_{12}^{(j)} \\ s_{21}^{(j)} & s_{22}^{(j)} \end{bmatrix} \begin{bmatrix} E_{\mathrm{A}}^{(j)} \\ E_{\mathrm{D}}^{(j)} \end{bmatrix} = \begin{bmatrix} i\kappa_j & \tau_j \\ \tau_j & i\kappa_j \end{bmatrix} \begin{bmatrix} E_{\mathrm{A}}^{(j)} \\ E_{\mathrm{D}}^{(j)} \end{bmatrix}. \tag{2.23}$$

Furthermore, the fields $E_{\mathrm{A}}^{(j)}$ and $E_{\mathrm{C}}^{(j+1)}$ (as well as $E_{\mathrm{B}}^{(j+1)}$ and $E_{\mathrm{D}}^{(j)}$) are related by a half-ring round-trip phase and loss accumulation,

$$E_{\mathrm{A}}^{(j+1)} = e^{[-\gamma/2+i\phi/2]} E_{\mathrm{C}}^{(j)} \tag{2.24}$$

$$E_{\mathrm{D}}^{(j)} = e^{[-\gamma/2+i\phi/2]} E_{\mathrm{B}}^{(j+1)} \tag{2.25}$$

$$j = 1, 2, 3, \ldots, N-1, \tag{2.26}$$

which allows the rewriting of the coupling matrix relation (2.23) to the transfer matrix form for each coupling region (that is, relating the

fields in the current ring with those of the previous ring),

$$\begin{bmatrix} E_{\mathrm{C}}^{(j)} \\ E_{\mathrm{D}}^{(j)} \end{bmatrix} = \begin{bmatrix} t_{11}^{(j)} & t_{21}^{(j)} \\ t_{12}^{(j)} & t_{22}^{(j)} \end{bmatrix} \begin{bmatrix} E_{\mathrm{A}}^{(j)} \\ E_{\mathrm{B}}^{(j)} \end{bmatrix}. \tag{2.27}$$

The components t_{nm}^{j} can be determined to be

$$t_{11}^{(j)} = s_{11}^{(j)} - \frac{s_{12}^{(j)} s_{21}^{(j)}}{s_{22}^{(j)}} = \frac{i}{\kappa_j} \tag{2.28}$$

$$t_{12}^{(j)} = \frac{s_{12}^{(j)}}{s_{22}^{(j)}} = \frac{\sqrt{1-\kappa_j^2}}{i\kappa_j} \tag{2.29}$$

$$t_{21}^{(j)} = -\frac{s_{21}^{(j)}}{s_{22}^{(j)}} = -\frac{\sqrt{1-\kappa_j^2}}{i\kappa_j} \tag{2.30}$$

$$t_{22}^{(j)} = \frac{1}{s_{22}^{(j)}} = \frac{-i}{\kappa_j} \tag{2.31}$$

and since eqns. (2.24) and (2.25) give relations to the quantities in the next coupling region, the following equations that relate the input fields in one region to the input fields of the next coupling region can be derived,

$$\begin{bmatrix} E_{\mathrm{A}}^{(j+1)} \\ E_{\mathrm{B}}^{(j+1)} \end{bmatrix} = T_j \begin{bmatrix} E_{\mathrm{A}}^{(j)} \\ E_{\mathrm{B}}^{(j)} \end{bmatrix} = \begin{bmatrix} e^{[-\gamma/2+i\phi/2]} t_{11}^{(j)} & e^{[-\gamma/2+i\phi/2]} t_{12}^{(j)} \\ e^{[\gamma/2-i\phi/2]} t_{21}^{(j)} & e^{[\gamma/2-i\phi/2]} t_{22}^{(j)} \end{bmatrix} \begin{bmatrix} E_{\mathrm{A}}^{(j)} \\ E_{\mathrm{B}}^{(j)} \end{bmatrix}, \tag{2.32}$$

where T_j is the properly defined transfer matrix for one step in the system. The entire system transfer matrix T can be obtained as the product of the individual step transfer matrices as

$$\begin{bmatrix} E_{\mathrm{A}}^{(N+1)} \\ E_{\mathrm{B}}^{(N+1)} \end{bmatrix} = T_N T_{N-1} \dots T_2 T_1 \begin{bmatrix} E_{\mathrm{A}}^{(1)} \\ E_{\mathrm{B}}^{(1)} \end{bmatrix} \equiv T \begin{bmatrix} E_{\mathrm{A}}^{(1)} \\ E_{\mathrm{B}}^{(1)} \end{bmatrix}. \tag{2.33}$$

The end goal of this computation is to obtain a scattering matrix for the system, i.e. expressing the output fields as functions of the

input fields. Noting that the coupling region $N+1$ does not exist, we make the following identification,

$$\begin{bmatrix} E_{\mathrm{A}}^{(N+1)} \\ E_{\mathrm{B}}^{(N+1)} \end{bmatrix} = \begin{bmatrix} E_{\mathrm{C}}^{(N)} \\ E_{\mathrm{D}}^{(N)} \end{bmatrix} = T \begin{bmatrix} E_{\mathrm{A}}^{(1)} \\ E_{\mathrm{B}}^{(1)} \end{bmatrix}, \tag{2.34}$$

which can be inverted (similarly to when eq. (2.23) was converted to eq. (2.27)) to for the system scattering matrix S.

Performing the calculation relating the drop/through ports to the input/add ports,

$$\begin{bmatrix} E_{\mathrm{C}}^{(N)} \\ E_{\mathrm{B}}^{(1)} \end{bmatrix} = \begin{bmatrix} S_{11} & S_{21} \\ S_{12} & S_{22} \end{bmatrix} \begin{bmatrix} E_{\mathrm{A}}^{(1)} \\ E_{\mathrm{D}}^{(N)} \end{bmatrix}, \tag{2.35}$$

where the components S_{ij} are related to the components of the system transfer matrix T_{ij} as

$$S_{11} = T_{11} - \frac{T_{21}T_{12}}{T_{22}} \tag{2.36}$$

$$S_{12} = \frac{T_{12}}{T_{22}} \tag{2.37}$$

$$S_{21} = -\frac{T_{21}}{T_{22}} \tag{2.38}$$

$$S_{22} = \frac{1}{T_{22}}. \tag{2.39}$$

The drop and through port transmission intensities can then be obtained as $|S_{11}|^2$ and $|S_{21}|^2$ respectively provided no add field ($E_{\mathrm{D}}^{(N)} = 0$) is excited, an example of which is shown in figures 2.8 and 2.9. The complex lineshape of such a CROW is the convolution of several add-drop lineshapes which yield a stacked effect. Also, the group delay corresponds with the resonances for the through and drop ports with pulse delays at the drop port and pulse advancements at the through port.

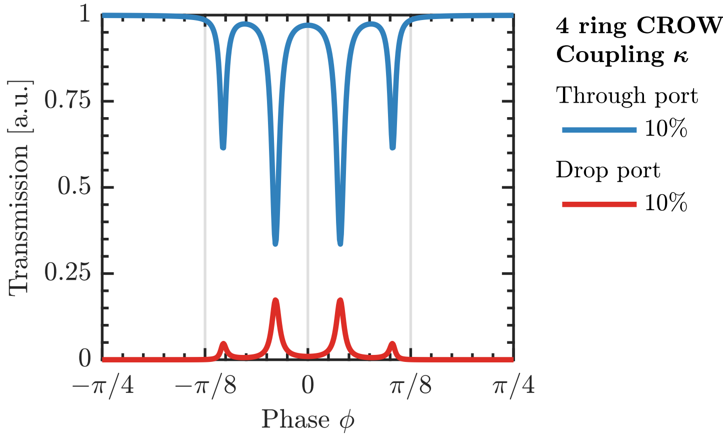

Figure 2.8: *Transmission spectra following eq.* (2.35) *for the through and drop ports of a 4 ring CROW. The coupling parameters were taken to be* $\kappa_j^2 = 0.1$*. Note the convoluted lineshape. The propagation loss corresponds to* 1.7 dB/cm.

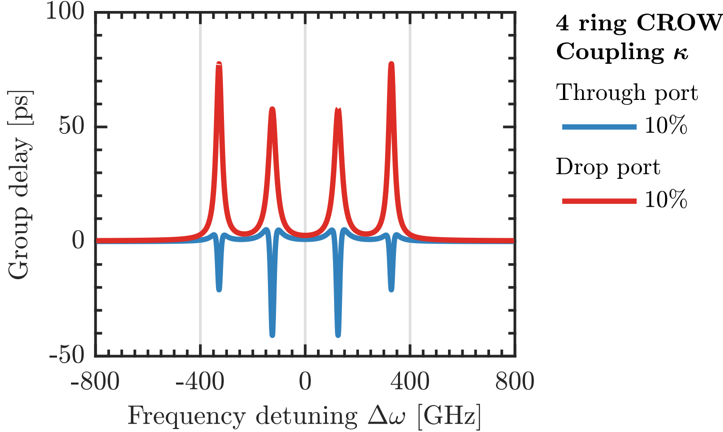

Figure 2.9: *Group delay as a function of frequency detuning (one-to-one correspondence with phase) for* 40 µm *radius CROW with the effective index* $n_{\text{eff}} = 1.7$ *and the same parameters as in figure 2.8. Once again, we see corresponding lineshapes with the transmission for the through and drop ports.*

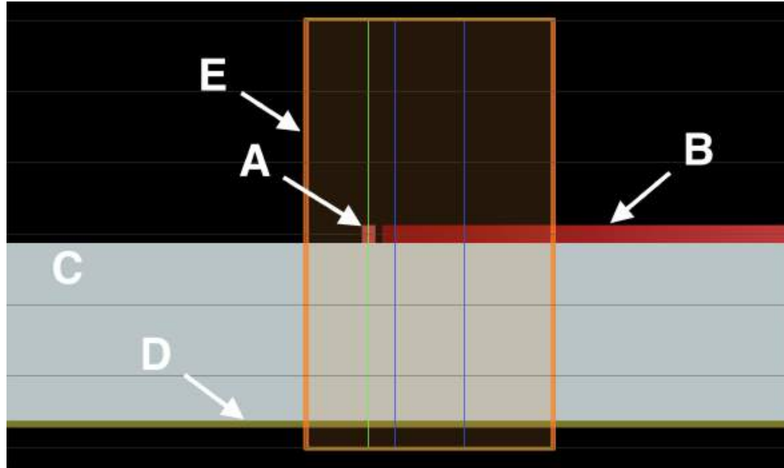

Figure 2.10: *Simulation stack setup with the bus waveguide (A), ring waveguide (B), substrate (C) and gold layer (D) enclosed in the simulation region (E).*

2.3 Numerical simulations

2.3.1 Coupling strengths

A theoretical estimate of the coupling (the coupling and the transmission coefficients) for a coupling region can be obtained by FDTD (finite-difference time-domain) simulations of the coupling region. This region is conceptually equal to a directional coupler with an excited input port and three output ports. Numerically, the simulation region is discretised into small parts (called meshing), and the number of nodes (number of small parts) effectively control the simulation complexity. As the coupling region is relatively large (in our case spanning approx. 40 µm x 40 µm x 5 µm) compared to the maximum node size (which for resolving a electromagnetic wave needs to be on the order of a wavelength or less), a full 3D simulation quickly consumes all available memory or takes a very long time.

To mitigate this, a 2.5D simulation variational solver (varFDTD) was employed, which computes the effective stack refractive index across the depth dimension and then carries out a normal 2D simu-

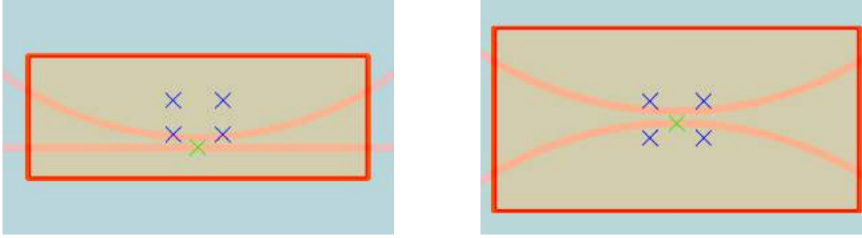

Figure 2.11: *View from above of a straight (left) and bent (right) bus waveguide coupling region. The rectangular area is the simulation domain.*

lation iteratively motivated by the planar structure. In this fashion, the advantage of the complexity reduction that a 2D simulation offers with respect to a 3D simulation is gained while still keeping the accuracy of the 3D simulation by allowing for out-of-plane field component propagation.

The simulation region model is set up as shown in figures 2.10 and 2.11. One bus waveguide is connected to another waveguide of identical dimension (800 nm wide and 250 nm high), separated by a varying distance in the range 10 nm to 400 nm. The simulations were carried out for both a straight bus waveguide coupled to a ring, and also a ring bus waveguide coupled to a ring (all bends with radius 40 µm.

Modal simulations (i.e. solving for the eigenmodes of the structure as discussed in section 2.1) was carried out to identify the fundamental transverse electric (TE) and transverse magnetic (TM) modes and their corresponding propagation constants. These fundamental modes were then selected as the input fields for the simulations, and by a feature of the solver of choice (MODE Solution®, Lumerical Inc, 2019), these could be directly excited at the input port. Furthermore, the solver can account for the effects a bent waveguide has on the mode so that these could be excited directly in the case of the ring-ring simulation.

By normalising the power propagating out of each of the output ports with respect to the excited power at the input port, the effective power coupling and transmission coefficients of the coupler can be

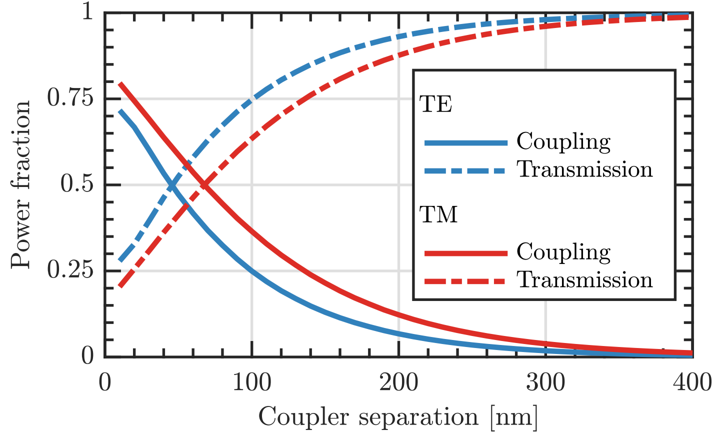

Figure 2.12: *Numerical power coupling and transmission fractions as a function of coupler separation for the fundamental TE and TM modes for a **straight waveguide bus**.*

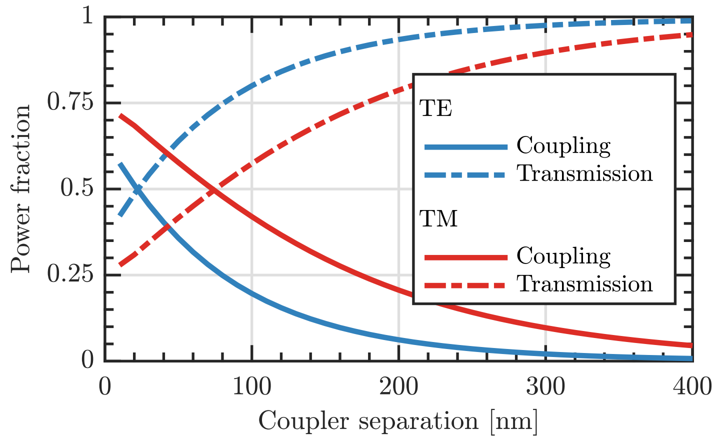

Figure 2.13: *Numerical power coupling and transmission fractions as a function of coupler separation for the fundamental TE and TM modes for a **bent waveguide bus**.*

calculated for each of the separations. These results are shown in figure 2.12 for straight bus coupling and in figure 2.13 for bent bus coupling but can be summarised as follows:

1. The TM modes generally have higher coupling coefficients than the TE modes (as expected as TM modes suffer larger mode delocalisation in bent waveguides than TE modes),
2. Practically power coupling strengths between 0 and ≈ 0.5 can be obtained (as resolving gaps below 50 nm imposes some fabrication difficulties), with slightly lower coupling with bent bus waveguides.

2.3.2 Time domain models of CROWs

The transfer matrix models of CROWs presented in section 2.2.3 works very well for determining the frequency responses of the systems at a fixed angular frequency ω corresponding to a certain wavelength λ. However, these methods were developed under the assumption of strictly linear time-invariance (LTI), and therefore falls short on accurately describing dynamical behaviour.

The important timescale is the order of the cavity photon lifetime (usually around picoseconds) where dynamical behaviour on that order or faster must be treated in a pure time domain model, whereas behaviour much slower than this can be considered as pseudo-LTI systems. In this thesis, none of the tuning methods employed occur on timescales fast enough to require pure time domain methods but they are nonetheless not entirely time invariant. Therefore, an alternative method to the transfer matrix method (or rather a generalised time domain version of it) is also presented.

For a time discretisation, the idea is to divide the propagation distance of the system into the small segments of equal length Δl. The discretised time steps are then taken to be the time required to propagate that length for the envelope of the light,

$$\Delta t = \frac{\Delta l}{v_g} = \Delta l \frac{n_g}{c}. \tag{2.40}$$

By then taking the fields at successive nodes to be the field at the previous node at a previous time step multiplied by the phase

shift and loss associated with the propagated distance at that specific time, an accurate model is obtained. Modelling CROWs with uniform radius R, we take the time step to be the time taken for the envelope to propagate half a ring, i.e.

$$\Delta t = \pi R \frac{n_g}{c}, \tag{2.41}$$

and furthermore model the interaction regions (the directional couplers between two successive rings) to have zero length and instantaneous field transfer according to equation (2.23).

Initially, a pulse (or any desired field shape) is injected in the input port $E_{\mathrm{A}}^{(1)}(t)$ (we now assume that there is no add field), and then at every time step $t_k = k\Delta t$,

$$1. \quad E_{\mathrm{A}}^{(j+1)}(t_k) = E_{\mathrm{C}}^{(j)}(t_{k-1}) e^{[-\gamma+i\phi]/2} \tag{2.42}$$

$$2. \quad \begin{bmatrix} E_{\mathrm{B}}^{(N+1)}(t_k) \\ E_{\mathrm{C}}^{(N+1)}(t_k) \end{bmatrix} = \begin{bmatrix} \tau_{N+1} E_{\mathrm{A}}^{(N+1)}(t_k) \\ i\kappa_{N+1} E_{\mathrm{A}}^{(N+1)}(t_k) \end{bmatrix} \tag{2.43}$$

$$3. \quad E_{\mathrm{D}}^{(j)}(t_k) = E_{\mathrm{B}}^{(j+1)}(t_{k-1}) e^{[-\gamma+i\phi]/2} \tag{2.44}$$

$$4. \quad \begin{bmatrix} E_{\mathrm{B}}^{(l)}(t_k) \\ E_{\mathrm{C}}^{(l)}(t_k) \end{bmatrix} = \begin{bmatrix} \tau_l & i\kappa_l \\ i\kappa_l & \tau_l \end{bmatrix} \begin{bmatrix} E_{\mathrm{A}}^{(l)}(t_k) \\ E_{\mathrm{D}}^{(l)}(t_k) \end{bmatrix} \tag{2.45}$$

$$5. \quad t_{k+1} = t_k + \Delta t, \tag{2.46}$$

where the indices j, l

$$j = 1, 2, 3, \ldots, N \tag{2.47}$$

$$l = N, N-1, N-2, \ldots, 1, \tag{2.48}$$

are summed over at each time step and the previously time-invariant phases and losses ϕ, γ now take on the more general, time and spatially dependent, form

$$\phi \equiv \phi(t, \lambda) \tag{2.49}$$

$$\gamma \equiv \gamma(t, \lambda). \tag{2.50}$$

Figure 2.14 shows an example from using the derived numerical algorithm for a 9 ring ($N = 10$) ring CROW with uniform coupling constants $\kappa = 0.1$ and propagation loss 1.7 dB/cm highlighting the delay of the drop-port pulse as well as the through-port pulse. The simulation probe detuning was chosen to highlight the maximum drop port delay, hence the negligible through port delay.

For code snippets using the transfer matrix and time domain models, see Appendix D.

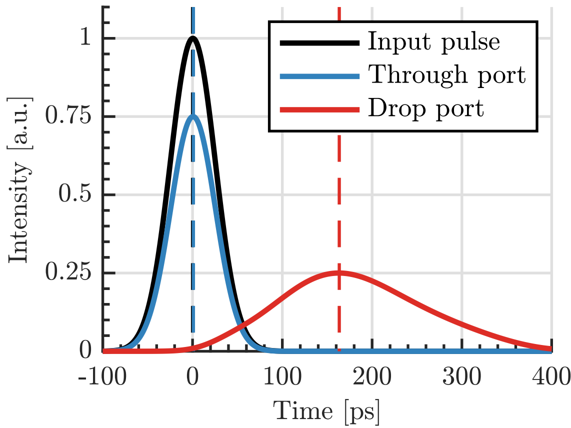

Figure 2.14: *Numerical time-domain simulation for a 9 ring ($N = 10$) ring CROW (40 µm radius) following the algorithm laid out showing the (normalised) intensities at the through and drop ports. The simulation was initialised using a 10 ps variance Gaussian input pulse and the inter-ring coupling taken to be uniformly $\kappa = 0.1$.*

3 Fabrication and characterisation

3.1 Technology of nanofabrication

Here, some of the main technologies used in the photonic chip fabrication process are presented.

3.1.1 Lithography

All fabrication involves the transfer of a desired pattern from for example a CAD program to a minuscule chip. Lithography is one way of achieving this, and it works by selectively illuminating a light-sensitive photomask (called resist) placed on top of the sample. After the exposure, the sample is placed in a chemical developer that, depending on the type of the resist, either washes away the exposed resist or the unexposed resist. Using a negative resist means that the pattern of the photomask is not removed (i.e. the unexposed resist is washed away) and conversely using a positive resist means that the pattern of the photomask is removed (i.e. the exposed resist is washed away) as shown in figure 3.1.

Traditionally, optical lithography, that is, lithography where the resist is sensitive to the optical spectrum of light has been used for device fabrication. However, the resolution of a lithography system scales linearly with wavelength (the Rayleigh criterion), which limits optical lithography to patterns with details no smaller than microscale. Therefore, electron beam lithography (EBL), where the resist used is sensitive to electron radiation, is mainly used today for

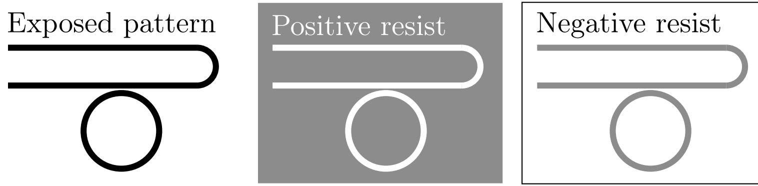

Figure 3.1: *Schematic representation of the result (shown in gray) from an exposed pattern (black, left) on a positive resist (centre) and a negative resist (right) after exposure and chemical development.*

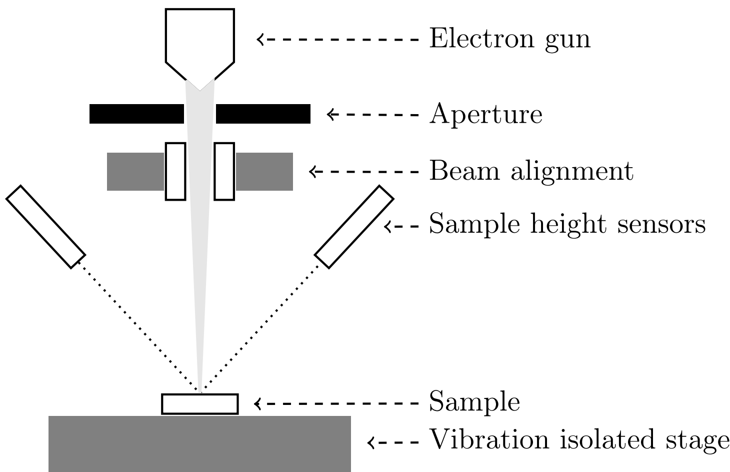

Figure 3.2: *Schematic illustration of the main components in an electron beam lithography system.*

increased resolution. A schematic of an EBL system is shown in figure 3.2.

The increased resolution of an EBL system comes at the cost of the writable area (commonly called the *write field*) of the system. As the beam control system can only move the electron beam so far, the structures that are to be patterned are divided into several write fields, each of which are written separately. When the system has finished writing one field, the movable stage moves the next write field into the writable area of the beam. This mechanical movement of the sample makes the system susceptible to so-called *stitching errors*, which

is when there is an, albeit small, mismatch between two neighbouring write fields. This has devastating consequences for waveguide-like structures that span several fields and are highly sensitive to cross-sectional mismatches as they serve as unwanted scattering centres. Furthermore, small structures that rely on precise periodic structures, such as gratings or other periodic devices, are also very sensitive to stitching errors as they, in that case, introduce unwanted phase shifts. One therefore has to take the write field size into account when designing the patterns that are to be written and make sure that the write field boundary (if possible) ends up in non-critical areas or simply to keep the (critical) design smaller than one write field.

Another technique to mitigate stitching errors is to employ a fixed-beam-moving-stage scheme, where, as the name suggests, the beam is held in place and the stage moves continuously. This is an excellent approach for long, isotropic structures that can be written in such a continuous manner but does not work well for other structures (especially structures with small features). A fully functioning EBL system contains many advanced techniques and processes to mitigate writing errors, and for example, laser interferometry is used as height sensors which work in conjunction with piezoelectric pillars that the sample rests on top of making height adjustments of the sample possible.

In this thesis, all devices were fabricated at the AlbaNova Nanofabrication Facilities using their EBL system VOYAGER (© Raith Nanofabrication GmbH) with a 50 kV electron gun and write field of 500x500 μm^2.

3.1.2 Etching

After a pattern has been transferred from a CAD design to the resist using a lithography process, it must be etched to transfer the pattern from the resist layer to the substrate itself. Simplistically, etching consists of exposing the sample to chemical and/or physical etchants causing areas not protected by the etch-resistant resist remaining from the lithography process to be sputtered (knocked) away.

Usually, one distinguishes between dry and wet etching, where the former uses a gas or plasma etchant while the latter uses a liquid etchant. The primary task of the etching process is to reliably transfer a given pattern to an underlying structure and the two most important

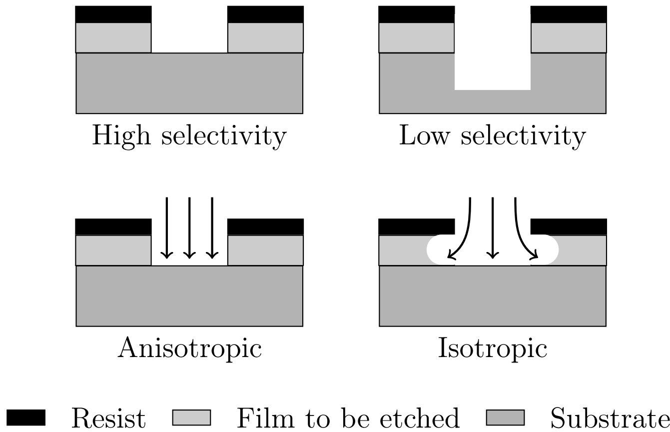

Figure 3.3: *Schematic illustration of the etching figure of merits selectivity and isotropy. Selective etchants will only etch the film that is to be etched and not the underlying materials, and an isotropic etch will etch in all directions, undercutting the mask and causing non-vertical sidewalls. Ideally, high selectivity and anisotropy is preferred.*

characteristics of such a process therefore is its selectivity and isotropy as shown in figure 3.3.

A highly selective etching will only etch the material that is to be etched and the underlying substrate, while a non-selective etching also etches at the substrate. Selectivity is usually not a problem for wet etching as the proper chemical etching agent choice results in only the film being etched, whereas physical bombardment of particles (dry etching), generally lacks selectivity.

The isotropy of an etch is a measure of the directionality of the etching. A low-isotropic etch (or an anisotropic etch) is highly directional and therefore etches only in the vertical direction hence producing vertical sidewalls and (in the ideal anisotropic case) perfectly transfer the resist pattern to the underlying film. Isotropic etches will etch in all directions, usually undercutting the mask resulting in an imperfect pattern transfer, but most critically resulting in non-vertical sidewalls which (in many photonic circuit applications) is fatal to the final functionality. Wet etching usually suffers from high isotropy and is therefore not a good choice for reliable photonic circuit fabrication.

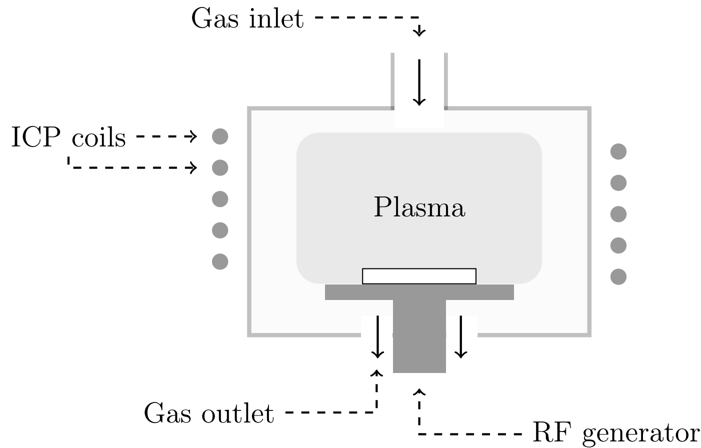

Figure 3.4: *Schematic of the ICP-RIE principle where the ICP coils surrounding the chamber excites the plasma separately from the RF field that controls the bombardment of the sample. Gas inlets and outlets are also shown, and the entire chamber is usually near-vacuum and held cold during operations.*

The most commonly used dry etching technique is Inductively Coupled Plasma Reactive Ion Etching (ICP-RIE) wherein a plasma is generated in a low-temperature near-vacuum setting and consequently used to bombard the sample. This technique is neither entirely chemical (selective and isotropic) nor physical (non-selective and anisotropic) etching, but rather a combination of the two. The ion bombardment from the plasma yields high impact sputtering (physical etching), while the proper choice of the constituents of the plasma can enhance the process by chemical reactions. Therefore, the resulting process is both selective and anisotropic.

As depicted in figure 3.4, the ICP-RIE principle builds on the idea of separating the plasma generation and the upwards and downwards movement of the ions and electrons. The ICP coils inductively excites the inserted gas and creates a plasma. By controlling the ICP power, one therefore controls the plasma ion concentration. The RF generator on the other hand generates a vertical electrical bias that causes vertical ion and electron movement and the ions are attracted to the

sample by applying a negative voltage bias on the sample pillar. The key difference between ICP-RIE and regular RIE is the decoupling of the ICP and RF field generation hence giving separate control of plasma density and ion bombardment energy.

In this thesis, an Oxford PlasmalabSystem 100 was used for all etching.

3.1.3 Plasma enhanced chemical vapor deposition

Similar to how ICP-RIE etching works, the same principles can be applied for thin-film deposition. Plasma enhanced chemical vapor deposition (PECVD) works by an RF field generating a plasma of the injected gases which then chemically react. Following the reaction, the plasma is deposited onto the sample naturally as it is located on the ground terminal of the RF field.

PECVD is usually employed when the thermal budget for the sample is low as it requires no to low (≈300 °C) heating in contrast to LPCVD (usually above 700 °C), and because of the addition of electrical bias, more uniform depositions can be achieved.

The PECVD processes in this thesis was carried out by our collaborator Iman Esmaeil Zadeh, PhD, at TU Delft in their nanofabrication facilities.

3.1.4 Electron-beam physical vapor deposition

Another way of depositing thin films of materials is by the means of E-beam PVD, where the idea is to accelerate electrons produced by an electron beam to high kinetic energies, which then is transferred to the evaporation material on impact, thus heating the sample and eventually causing it to vaporise in a vacuum chamber. EBPVD is a line-of-sight deposition method, meaning that the vapour coats everything in its line of sight in the chamber, and to achieve uniform deposition rates over the sample surface area one must ensure somewhat uniform heating of the evaporation material. A schematic drawing of an EBPVD system is shown in figure 3.5.

One way of achieving this is by randomising the movement of the beam impact spot on the evaporation material. Commonly, sweep controls for this are available whereby the effective beam impact spot

can be enlarged to cover a larger part of the evaporation crucible. Such control is achieved by altering the controlling magnetic field which then alters the electron beam deflection and thus impact position.

The electron beam is generated by a tungsten filament giving away electrons which are then accelerated by a high voltage power supply and then bent towards the evaporation material container (called crucible). To prevent overheating of the system itself the crucible and surroundings are water cooled which ensure that only the evaporation material is evaporated.

For higher uniformity depositions, the sample mount can be set to rotate, however at the cost of lower deposition rates. The converse technique is also commonly applied, when the uniformity is not of that great importance, the sample mount can be held fixed over the crucible with increased deposition rates.

Our facilities provide an Edwards Auto 306 with a FL400 front loading chamber for EBPVD fabrication.

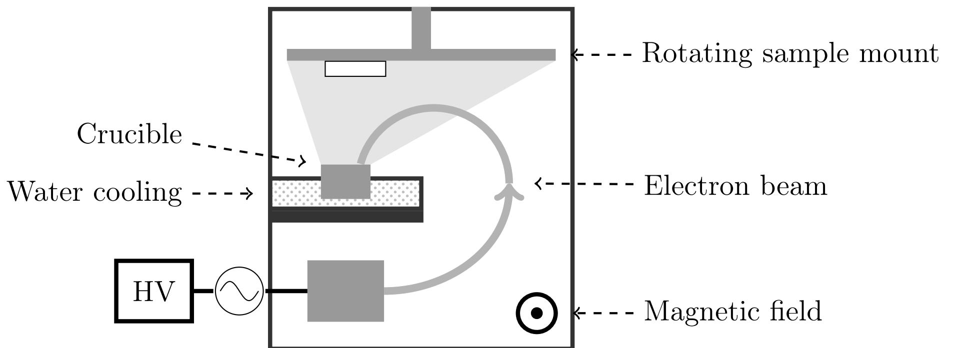

Figure 3.5: *Schematic of an EBPVD system showing a sample mounted on a rotating mount in the vapour created from the heated evaporation material contained in the water-cooled crucible.*

3.2 On-chip device fabrication

In this section, the workflow for device fabrication and the specific recipes are presented as shown in figure 3.6. As the piezoelectric

PMN-PT chips are expensive and fragile, all structures were prototyped on the much more available and cheaper pure silicon carrier wafers, that nevertheless had the same stack structure and similar fabrication processing. Hence, the general fabrication process is first presented, followed by the specifics and additional steps the piezoelectric wafer requires.

A1: Carrier wafers

The fabrication process itself began with commercially carrier wafers that served as the substrate on top of which the nanoscale devices are fabricated. For prototyping, pure silicon wafers were used as substrates (A1), where gold contacts were deposited by thermal evaporation, approximately 100 nm thick (A2). The gold contacts serve no other purpose in the prototype than to make the stack similar to the piezoelectric chip for testing optical properties and characterising device losses as they are used to apply the piezoelectric strain for tuning the devices on the piezoelectric chip. Therefore, only the top contact was deposited on the prototype stack to conserve processing time.

For the real stack, the process began with commercially available PMN-PT wafers that were delivered with one side already polished and therefore needed gold contact deposition on both the top and bottom realised through thermal evaporation (A2).

A2: EBPVD gold contact deposition

To reliably deposit the rest of the stack, the surface roughness of the gold contact layer (and the underlying substrate) is very important, and polishing the samples is one approach to reduce this roughness. The company provided chip is delivered already polished on one side, while the in-house chips were unpolished.

For the deposition of the gold contacts, electron-beam physical vapor deposition was used. Before beginning, the sample was cleaned in acetone (for silicon chips) or isopropanol (PMN-PT) manually.

After that, the sample was glued to the sample holder using an old photoresist (S1818), and the sidewalls painted with the same photoresist. This was done to ensure that no gold bonded to the sidewalls, which in the end would cause a short circuit between the top and

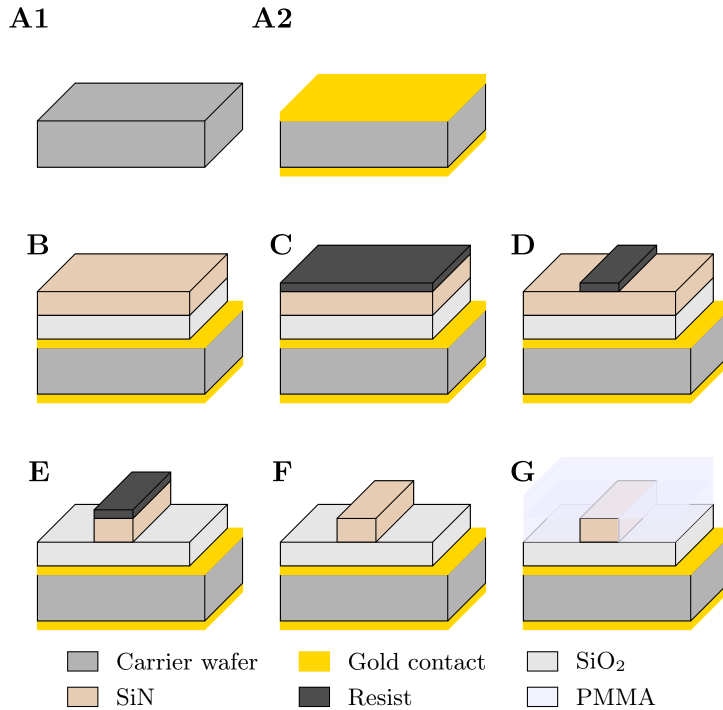

Figure 3.6: *Fabrication process for on-chip devices.* ***A1/2:*** *Diced carrier wafer with and without cold contact,* ***B:*** *SiO_2 and SiN PECVD deposition,* ***C:*** *lithography resist application,* ***D:*** *electron beam lithography patterning,* ***E:*** *pattern transfer to SiN by dry etching followed by,* ***F:*** *chemical removal of residual resist and finally,* ***G:*** *PMMA cladding application.*

bottom gold contacts. Furthermore, the photoresist used as glue has excellent bonding strength when soft-baked and can be removed easily afterwards.

Following the photoresist application, the sample was soft-baked on a hot plate slowly ramped up to 90 °C to drive the resist out of solution.

The sample was then mounted in the evaporation chamber, a vacuum of 1 µbar pumped and then the deposition started. To ensure good adhesion of the Au, a very thin (10 nm) layer of the adhesion promoter chromium (Cr) was deposited first with non-rotating sample holder, tooling factor of 1.5 and a filament current of 26 mA which gave the final deposition rate 0.2 nm/s.

Following this, a 100 nm gold (Au) layer was deposited using non-rotating sample holder, a tooling factor of 1.5 and a filament current of 78 mA that gave deposition rates between 0.06 nm/s to 0.15 nm/s.

The lift-off procedure consists of an acetone bath followed by plier-assisted lift-off and cleaning with acetone and isopropanol.

To verify the quality of the deposition, the sample is investigated under microscope to look for any resist residue and also to check for gold residue on the side walls. If needed, any residue was scraped off with a scalpel, and to finish off a conductivity measurement was taken between the top and bottom gold contacts to verify that there was no short circuit.

B: PECVD SiO_2/SiN deposition

Keeping a corner or a side of the gold contact exposed, a 2 µm to 3 µm thick silicon oxide (SiO_2) base cladding layer was deposited using plasma enhanced chemical vapor deposition (PECVD).

To allow for the photonic device integration, a 250 nm to 330 nm silicon nitride (SiN) was deposited on top of the silica layer by the same process. This SiN layer introduces a refractive index contrast to the silica layer of around $\Delta n \approx 0.5$ making the stack suitable for photonics. Both of these PECVD processes was carried out by our collaborator Iman Esmaeil Zadeh, PhD, at TU Delft in their nanofabrication facilities.

The silicon dioxide deposition was carried out using SiH_4:N_2O (710 sccm:425 sccm) chemistry at 800 mTorr and the silicon nitride de-

position using SiH_4:NH_3 (800 sccm:16 sccm) chemistry at 650 mTorr. In both cases the sample temperature was held constant at 300 °C and a RF power of 24 W at 13.56 MHz was used, and the PECVD process was followed up by ellipsometry measurements to confirm the deposition thicknesses and refractive indices.

C: Lithography pre-processing

During the Si wafer processing, the stack usually develops a hydrophobic surface which may cause the resist to bond poorly resulting in inconsistent pattern transfers and overall loss of fabrication quality. To mitigate this, the stack was first exposed to a 2 min oxygen O_2 plasma (20 sccm) cleaning process in the ICP-RIE etching tool using a low RF power and 50 W ICP. In addition, an adhesion promoter (AR 300-80, AllResist®) was applied afterwards through spin coating at 4000 rpm and then baked at 90 °C for 2 min which optimised the bonding conditions for the resist.

After the stack had been prepared, the resist was applied through spin coating. For the purpose of this thesis, a negative electron beam/deep UV resist was chosen (ma-N 2403, micro resist technology®), which leaves an approximately 350 nm thick layer when spun at 4000 rpm[1]. Finally, the stack was baked again at 90 °C for 2 min.

D: Electron Beam Lithography

After resist application, the desired patterns were exposed using an EBL system (see figure 1.3 for an example pattern). All patterns were designed with the write field size limitations of the EBL system in mind keeping, if possible, the critical parts of the structure within one field. The structures were exposed in an array structure with a base dosage of 300 µC/cm^2 and a dose multiplier of 1.02 thus yielding several sets of the same structures with different dosages.

After writing, the resist is chemically developed using ma-D 525 (micro resist technology®) for 1 min and then rinsed in distilled water for 1 min. It is then cleaned using N_2 gas. The developing process leaves (in our case, using negative resist) the exposed pattern and removes the unexposed resist.

[1] according to the spin curve provided by the manufacturer.

E/F: Dry etching

Post-development, the sample must be etched to transfer the resist pattern to the substrate. Given our samples with a 250 nm to 330 nm SiN layer stacked on top of the SiO_2 substrate, we want to etch the full height of the SiN layer such that the only remaining silicon nitride is that which has been patterned. The etching process recipe used is as follows:

Firstly, the machine was loaded and brought to vacuum. The chamber temperature was then brought to and stabilised at 20 °C for at least 3 min. Then, the etching itself commenced with a CHF_3 (30 sccm), CF_4 (5 sccm), O_2 (5 sccm) gas mixture using 100 W of RF and ICP power each for a given time. Finally, the sample and chamber were flushed with a 20 sccm Ar gas for 2 min before the chamber was vented and sample unloaded.

As a final step in the etching process, the sample was cleaned, and any excess resist removed using mr-Rem 700 (micro resist technology®) followed by cleaning with acetone and isopropanol.

Etch depth profiling

In regular intervals, the etch depth needs to be profiled as the etching tool might not have a consistent etch rate over time. To determine the etch rate (i.e. the nm/min that the tool etches away), drops of resist are applied to the same substrate which is then baked at 90 °C for 10 min and subsequently etched for a fixed period of time. By surface profiling (KLA-Tencor P-15 Surface Profiler), the total etch depth is determined by averaging several measurements over several drops of resist and different scan directions which, by dividing by the etching time yield the etch rate.

As an example, the etch rate for SiN using the previously mentioned recipe was 77 nm/min 2019-03-26 and 72 nm/min 2019-05-31.

G: Cladding application

As a final step in the process, a cladding layer was added for extra protection of the circuits as well as to provide a better refractive index contrast between the silicon nitride devices and the surround-

ings. In this thesis, Poly(methyl methacrylate) (PMMA), or in common words, acrylic glass, was used. More specifically, PMMA A8 (MicroChem) was added to the cleaned newly-etched stack, spun at 2500 rpm and then baked at 90 °C for 2 min on a hot plate leaving >1 µm of cladding.

3.3 Piezoelectric device fabrication

After prototyping on silicon wafers, the final designs were fabricated on PMN-PT carrier wafers. The fabrication follows the same steps as for the silicon carrier wafers, with some extra caution due to PMN-PT being more fragile.

A: PMN-PT carrier wafers and gold contacts

The PMN-PT chips used in this thesis was not grown in-house but rather commercially available. Two chips were used, one from TRS Technologies (X2A, 200 nm thick, uncoated) and one from Crystal Material (500 nm thick, one side polished). Both crystals were cut in the (100) direction which gives the optimal piezoelectric performance.

Similar to the prototype chips, a 100 nm thick gold contact was deposited on the uncoated sides by thermal evaporation such that the final wafer is a carrier wafer with gold contacts on both sided to serve as the electrical contacts whereby the piezoelectric strain is induced.

The TRS chip served as a PMN-PT chip precursor and all fabrication was first carried out on it to mitigate all possible issues or complications. Following the prototyping on the TRS chip, the real fabrication was carried out on the Crystal Material chip.

B-G: Stack deposition and device fabrication

After the base wafer has been processed accordingly, the wafers were sent to Iman Esmaeil Zadeh at TU Delft for PECVD deposition of the silicon oxide and silicon nitride (B), and after their return to us, treated by the usual lithography and post-lithography steps (C-G) for device fabrication.

H: Piezoelectric poling

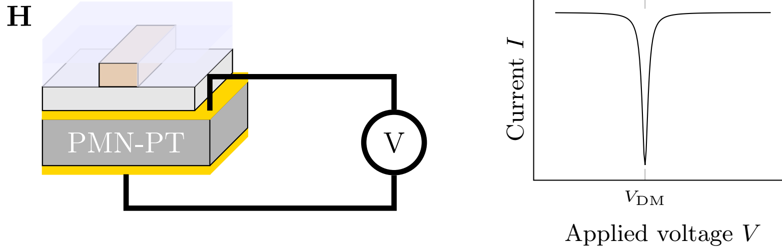

Figure 3.7: *Schematic of the piezoelectric poling process with the corresponding characteristic IV poling curve showing the domain switching at the domain-switching voltage* V_{DM}.

The one differentiating fabrication process between the silicon prototype chips and the PMN-PT piezoelectric chips was the post-processing step of electrical poling that needs to be carried out on piezoelectric chips.

Generally, the directionality of the domains of a piezoelectric material are not aligned, but rather distributed arbitrarily and the material as a whole therefore spontaneously polarised (unpoled PMN-PT is spontaneously polarised in the (111) direction). This leads to poor piezoelectric performance, and to make use of the full tuning potential, the domains needs to be aligned by poling.

The poling consists of applying a uniform electrical field over the crystal, slowly increased up to the material specific domain-switching voltage where the all domains of the crystal align with the external applied field. This switching behaviour is clearly visible in an IV curve (current-voltage), where a current peak appears when crossing the domain-switching voltage indicating the directional reassembling of the domains.

Figures 3.8 and 3.9 shows SEM images of fabricated devices following the recipes detailed in Chapter 3.

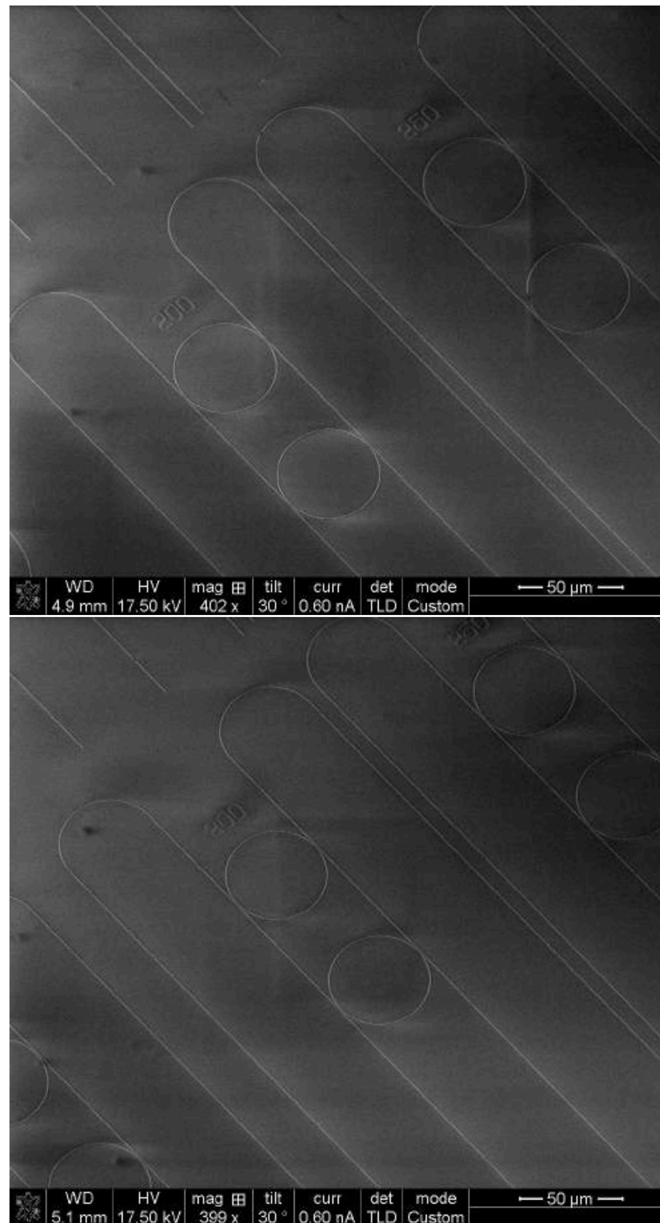

Figure 3.8: *SEM images of fabricated devices (figure continues on next page...)*

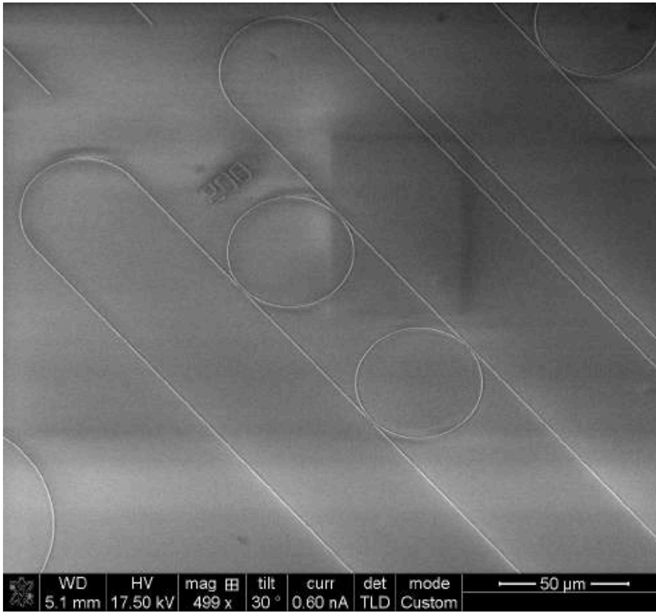

Figure 3.8: *SEM images of the fabricated EIT-configured ring resonators following the recipes laid out in Chapter 3 with* 200 nm *(left) and* 250 nm *wide coupling gaps.*

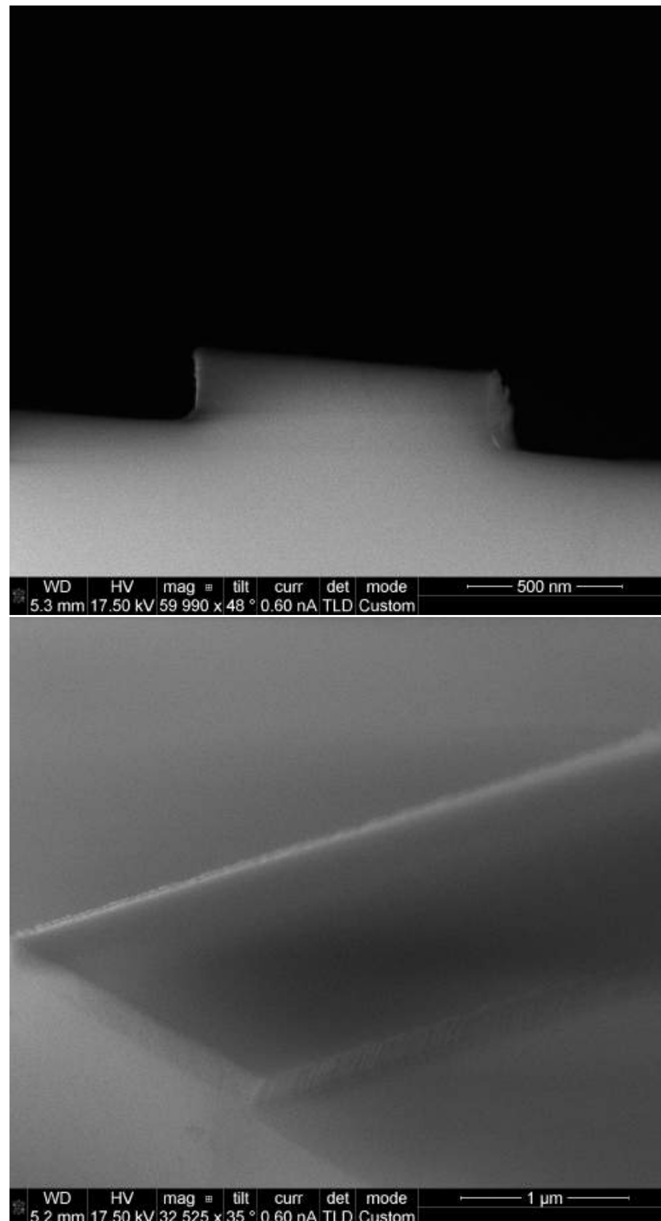

Figure 3.9: *SEM images of the fabricated resonators highlighting the sidewall profiles of the devices.*

3.4 Sample cleaving and mounting

After the outlined fabrication process and prior to measurements, the intermediate cleaving and mounting must take place.

Cleaving

Given the nature of the measurement setup used, the input excitation and output collection from the samples was achieved through butt coupling, whereby coupling is achieved by simply focusing light onto the edge of the device. This requires the input and output ports of the devices to be at the very edge of the chip, which presents a problem as they are fabricated as centred on the chip as possible to have highest stack uniformity and to mitigate many potential sources of failure, such as stitching errors or structure breaking from handling.

The devices are brought to the edge of the chip by cleaving the chip perpendicular to the waveguide direction. This is performed by scratching the sample and thus forming a natural starting point for the following crack propagation. The cleaving is then accomplished through applying pressure downwards on the scratch and intended crack while holding the rest of the chip fixed.

Cleaving as a process is not deterministic owing to the uncertainty of crack propagation which depends on things ranging from sample purity, local defects, crystalline defects to the pressure applied and the scratch depth and length. To prevent this from ruining a chip at this late stage in the fabrication process, the same structures were printed in a matrix several times hence forming at least a couple of possible cleaving locations should something fail.

Mounting

As the silicon chips require no special actuation for measurement, this section is dedicated for the steps taken to ensure that the piezoelectric samples can be actuated. Figure 3.10 depicts the finalised mounting of the sample.

The issue at hand is to connect the bottom and top gold contacts with externally exposed wiring which later will be connected to a voltage source. To achieve this, the sample was first glued onto a copper

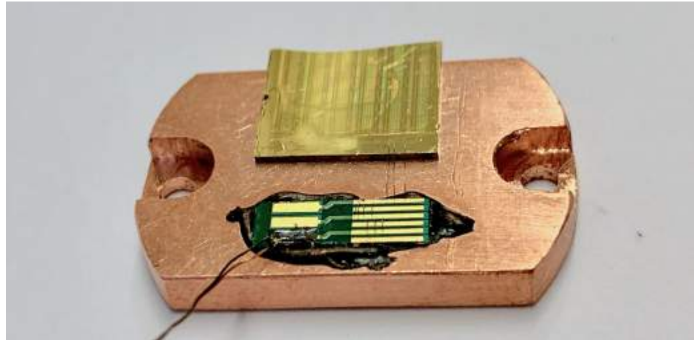

Figure 3.10: *Overview of the finished piezoelectric sample mounted on the carrier copper plate. For more detailed schematics, see Appendices A and B.*

sample holder slightly larger than the sample itself (approximately 20 mm x 15 mm) with a conducting silver glue, hence contacting the bottom contact.

At this stage, there is an important trade-off between the rigidity of the chip-to-copper holder bond and the freedom of movement for the chip. The piezoelectric actuation requires as much freedom of movement as possible to not limit the tuning range (as it expands/-contracts with applied voltage). The solution was to glue only one corner of the substrate to the holder with as little glue as possible to prevent glue creeping up along the substrate edge and thus possibly shorting the circuit by connecting the top and bottom gold contacts. Additionally, during the process the sample was not pressed down on the drying glue as it ensures that as little as possible of the substrate contacts the holder and reduces the risk of glue creeping.

Finally, to access the top contact, a PCB (printed circuit board) was glued onto the sample holder next to the chip using epoxy glue. This was done to allow sufficient space for soldering a wire for external access. In this fashion, the PCB is used as a bridge between the macroscopic external access and the microscopic chip contacting. The PCB is then connected to the top gold contact on the chip by using a wire bonder (Kulicke & Soffa Digital Wedge Bonder, 4523D) that attaches a 1 mm thick silver thread by an ultrasonic mechanism that melts the cable ends in place.

Details of the mounting can be found in Appendices A and B.

3.5 Room temperature chip characterisation

After devices had been fabricated, they needed to be characterised. The characterisation was primarily carried out in one process; transmission spectroscopy to investigate the spectral response in the wavelength domain, which was used both for the silicon substrates and the piezoelectric substrates.

3.5.1 Transmission spectroscopy

The transmission spectroscopy was carried out through laser butt coupling into the input port of the chip followed by the collection of the output port transmission that was rerouted to a spectrometer.

In the already-built setup, the input laser used was a high-powered super-continuum pulsed source (YSL Photonics, SC Pro 7) emitting wavelengths between 400 nm to 2400 nm, set at a 5 MHz repetition rate and using a moderate power of 5 % to 15 % of the maximum output power 10 W (varying in the range 1 mW/nm to 15 mW/nm over the spectrum).

The laser was then sent through a series of mirrors and irises ensuring proper alignment with the rest of the setup, followed by a number of tunable attenuation devices that helped ensure that the spectrometer CCD was not saturated.

After that, the beam path passed through a beamsplitter that divided the input and output parts of the setup, followed by a focusing objective (ThorLabs RMS40X, NA = 0.65) with a working distance of 0.6 mm for effective butt coupling of the fabricated devices.

By manually moving the sample attached to the XYZ stage, coupling to the desired port on the sample could be achieved.

The same objective collected the output signal which was directed to the output part of the setup by the beamsplitter. There, a similar setup of mirrors and irises allowed for aligning the output beam path with the entrance slit of the spectrometer. Before that, the beam passed through a polariser that linearly polarised the output followed

by a lens that helped with focusing and aligning the beam on the spectrometer slit.

For resolving the output signal, an Acton SP2750 spectrometer (Princeton Instruments), equipped with a 1200 lines/mm grating and tunable entrance slit was used. The entrance slit controls and the lens were used together to obtain the maximum resolution possible by recursive reduction of the slit size and beam focus point centring.

For the piezoelectric chips, a Keithley voltage source was added to the measurement setup and used as the tuning mechanism.

Finally, all data was collected using a LabView enabled computer controlling the spectrometer and voltage source.

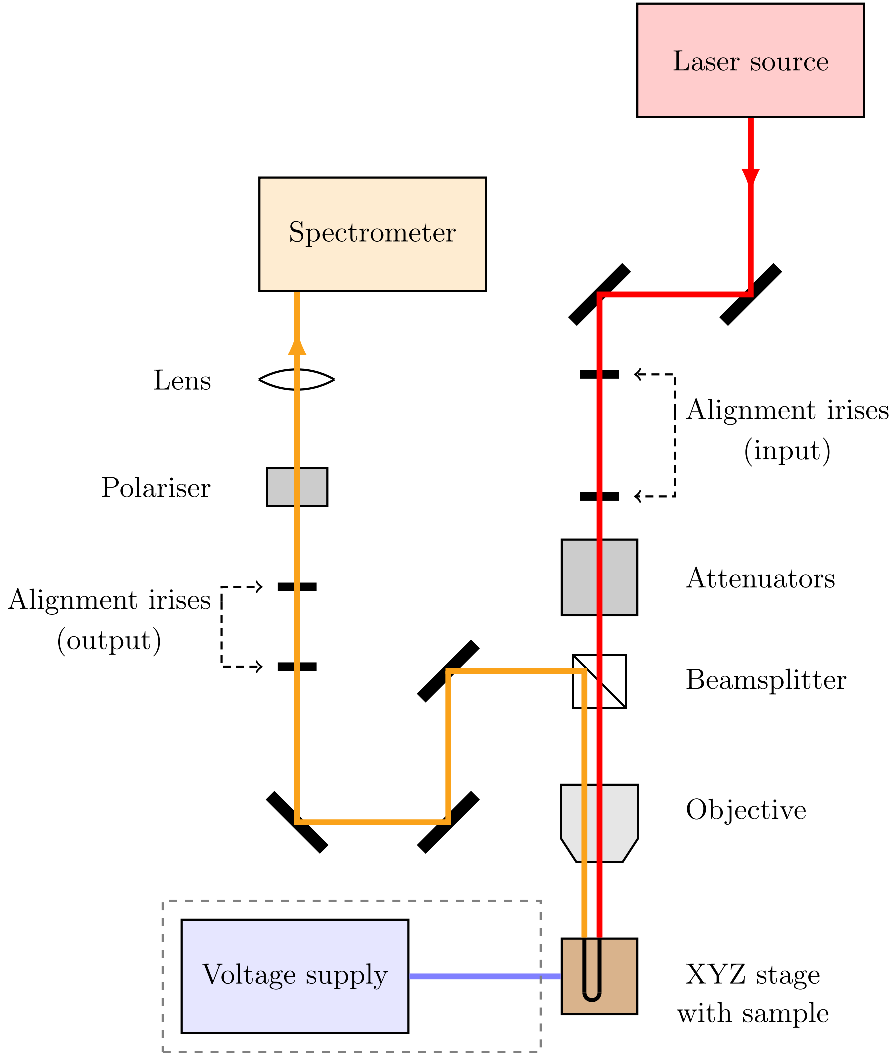

Figure 3.11: *Schematic drawing of the room temperature setup used for characterising the fabricated devices by transmission spectroscopy.*

4 | Results and analysis

Following the theoretical modelling of the structures, prototyping on silicon substrates was commenced. After several iterations finely altering system and fabrication parameters and characterising the device behaviour, the tunable piezoelectric substrate was used in fabrication. The main objective with the piezoelectric substrate was not to do the device characterisation, but rather to tune the already characterised and optimised devices. Unless otherwise specified, all devices were fabricated on 230 nm thick SiN with a standard waveguide width of 800 nm, designed to be single-mode at a wavelength of 900 nm.

4.1 Silicon substrates

The primary task of the silicon substrate prototyping was to determine the resonator quality and also to get a measure of the coupling factors related to the ring-bus waveguide separation, which by extension gives a measure of the range of obtainable circuit delays.

A variety of devices were patterned on silicon substrates including EITs, all-pass single rings, add-drop single rings and also all-pass and add-drop CROWs, but here only an excerpt of the results are presented.

For investigating the fabrication quality coupling strength of the ring resonator bus waveguide connections, a series of all-pass single rings with a 40 µm radius and varying coupling gap between 100 nm to 400 nm were fabricated. Figure 4.1 show the power extinction ratio, resonance width and the intrinsic quality factors of these rings around wavelengths of 800 nm, with the general take-away being resonance widths between 0.06 nm to 0.20 nm which yield Q-factors on

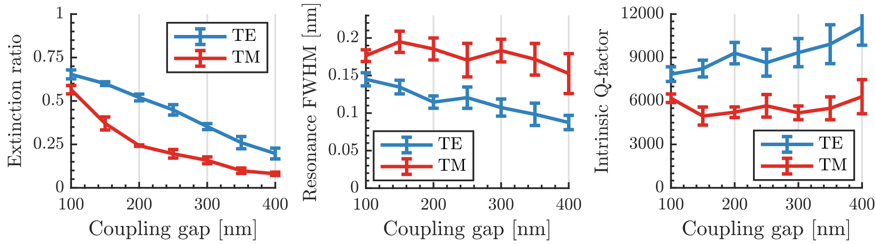

Figure 4.1: *Power extinction ratio (left), resonance width (FWHM) (middle) and intrinsic quality factor (right) as functions of the coupling gap for the TE and TM modes of all-pass single ring resonators around wavelengths of* 800 nm.

the order of $10^3 - 10^4$ and propagation losses below 5 dB/cm. The extracted propagation loss is an upper estimate as it takes into account the coupling region loss in addition to the intrinsic loss due to propagation.

Furthermore, the behaviour of the measured extinction ratio can be compared with those theoretically predicted (figure 2.12). Theoretically, the TM mode has a stronger coupling constant than the TE mode for a fixed gap size. However, the parameters that determine tangible transmission curves are mainly the waveguide and coupling losses for the propagating modes.

Therefore, the fact that the extinction ratio curve for the TM mode is higher than the TE curve in a window around wavelengths of 800 nm indicate that the TM mode is closer to the critical coupling regime than the TE mode there and thus encounter more coupling losses in the current measurement setup, albeit marginally. However, the overall measured transmission behaviour corresponds to the predicted one giving merit to both the fabricated devices and the theoretical model used.

Having first characterised the simpler all-pass cavities, we now move on to the add-drop configuration which additionally has a drop port from which we expect the largest delays and therefore we also highlight some results from an add-drop single ring resonator configuration. The same radius (40 µm) was used with the same (and in this case symmetric) coupling distances 100 nm to 400 nm in 50 nm steps

which when measured gave resonance widths of as low as 0.02 nm to 0.08 nm which translates to quality factors of between 10 000 to 45 000, losses below 5 dB/cm and experimentally extracted group delays around 30 ps.

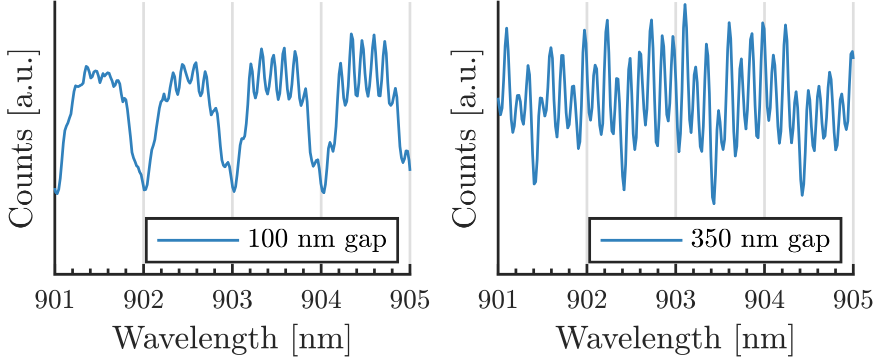

Figure 4.2: *TE resonances for add-drop cavities with symmetrical* 100 nm *(left) and* 350 nm *(right) coupling regions.*

The actual propagation loss is even lower than this, as the loss extraction builds on the fact that the ring only has one bus waveguide connections (as is the case for all-pass devices), while these figures were extracted for add-drop devices, that in addition has a second bus waveguide connection.

Excerpts of TE resonance spectra are shown in figure 4.2 for two coupling gaps with resonance widths in the range 0.05 nm to 0.15 nm.

Furthermore, figure 4.3 shows the measured spectral drop port resonances for a 2-ring CROW at two different coupling gaps (200 nm (blue) and 400 nm (red)) highlighting the spectral characteristics at two different spectral regimes fo the TE mode. These plots show the spectral variance of the resonances, and especially notice the difference in the extinction of the central troughs between the regime around 900 nm (top row) where it is principally extinct whereas around and below 800 nm (bottom row) it is not. This is due to the wavelength dependent coupling regimes, and in both coupling gap cases, the CROWs are closer to the critical coupling regime around 900 nm. Also, the mode splitting (i.e. the central trough width) grows with stronger coupling.

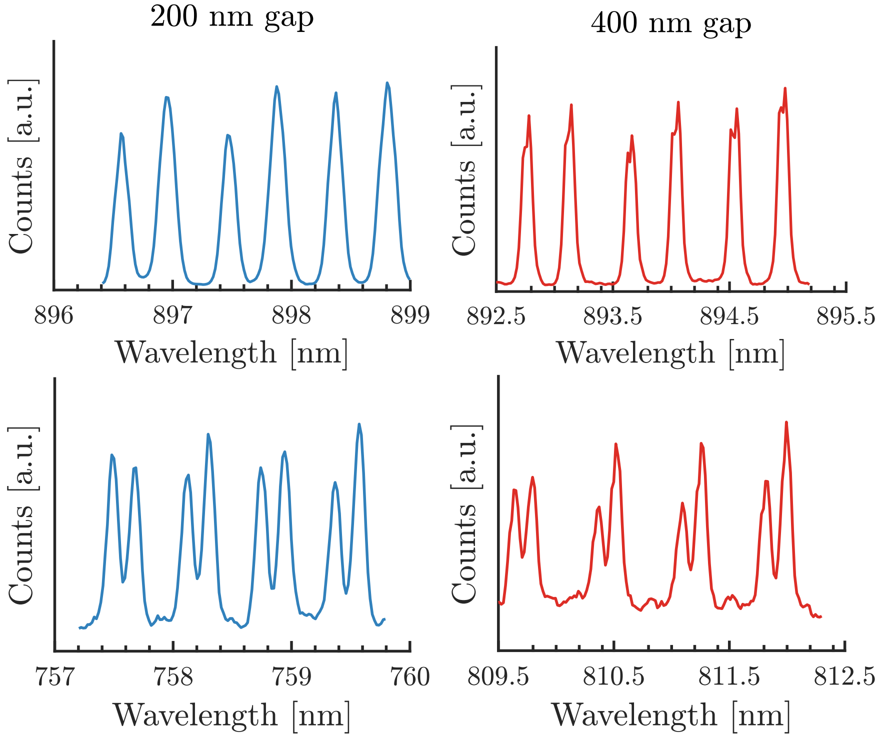

Figure 4.3: *TE resonances for a 2-ring silicon CROW at the coupling gaps* 200 nm *(blue, left column) and* 400 nm *(red, right column) for different spectral regimes (top and bottom rows). All figures span* 3 nm.

4.2 PMN-PT substrate

On the PMN-PT substrates, a set of devices were fabricated for investigation of the tuning. Firstly, two single-ring resonators with coupling distances of 200 nm and 250 nm and radii 40 µm were included for chip and fabrication process characterisation. In addition, a 5-ring CROW with the same radii and uniform coupling gap 200 nm was fabricated to characterise the circuit delay achievable.

The fabricated devices were first investigated using the transmission spectroscopy setup, which yielded the spectral responses shown in figures 4.4, 4.5, 4.7, 4.8, for the single ring resonators and the 5-ring CROW drop and through ports respectively.

The figures of merit for the single ring resonators are the resonance widths and extinction ratios, from which secondary parameters such as the Q-values can be extracted. Table 4.1 shows the extracted cavity parameters, which indicate (as expected) broader TM resonances

Coupling gap	Mode	FWHM [nm]	Q-value	Extinction ratio
200 nm gap	TE	0.145 ± 0.021	7825 ± 475	0.685 ± 0.108
	TM	0.185 ± 0.012	6728 ± 487	0.72 ± 0.142
250 nm gap	TE	0.161 ± 0.015	7268 ± 630	0.460 ± 0.110
	TM	0.209 ± 0.016	5515 ± 576	0.485 ± 0.109

Table 4.1: *Extracted cavity parameters from the single ring resonators on PMN-PT substrates around* 800 nm *wavelengths.*

compared to the TE resonances.

The extracted intrinsic quality factors are on the low side from what was expected to achieve (quality factors of 10000 or more are regularly achieved), which is a sign of there being sources of losses that are unaccounted for (with a measured propagation loss of below 15 dB/cm). For example, the waveguide roughness plays an important role in the quality factor of the cavities. Due to continuous maintenance of the etching tool small adjustments were made to the etching recipe which resulted in measurable increased waveguide sidewall roughness which may account for some of the losses. These adjustments were made as the original recipe also showed deterioration in the output quality of the sidewalls, but further optimisation of this step was outside the scope of this thesis.

However, it should be mentioned that during the time-frame the work of this thesis was conducted in, the reactive ion etching tool RF power supply suffered from severe ageing and deterioration resulting in the earlier devices fabricated (silicon devices used for prototyping) accurately reflecting the outcome of the standard etching recipe while the later devices (PMN-PT devices fabricated near the project end) suffered the consequences of the deteriorating equipment. Shortly after the project end the RF generator actually went out of commission and had to be replaced in its entirety by the AlbaNoba Nanofabrication Facility.

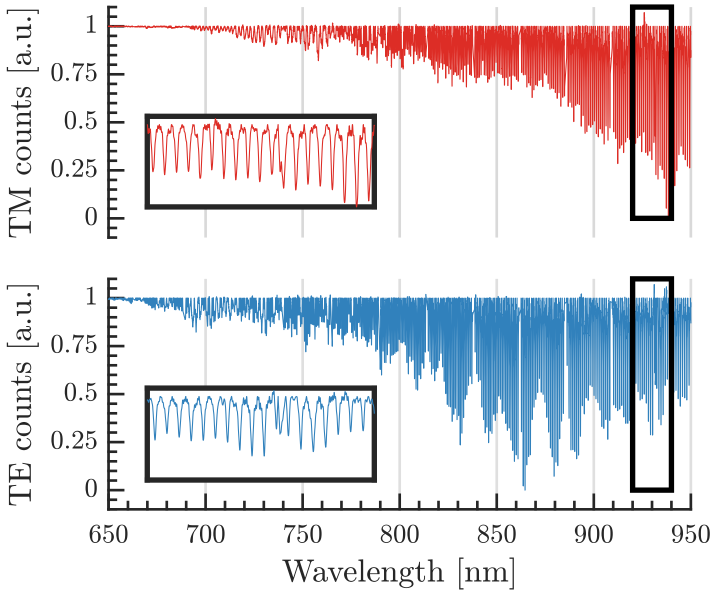

Figure 4.4: *Flattened TE and TM spectral response for a single ring resonator on a PMN-PT substrate with a* 200 nm *coupling distance.*

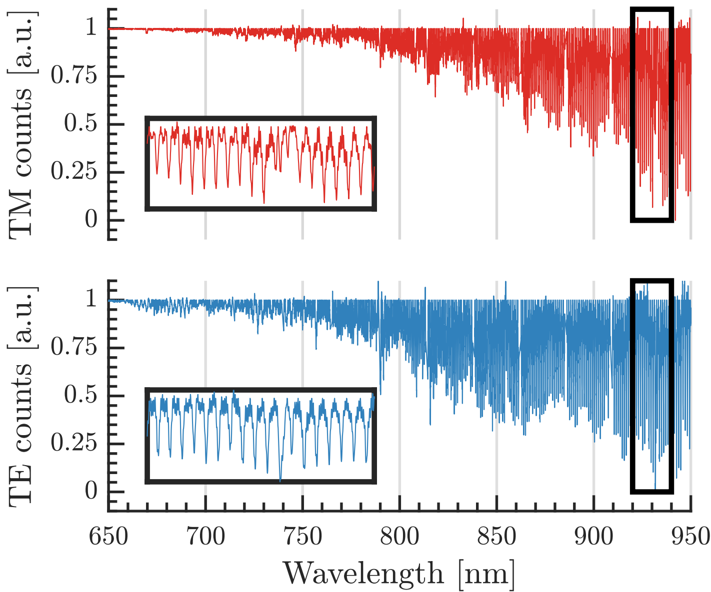

Figure 4.5: *Flattened TE and TM spectral response for a single ring resonator on a PMN-PT substrate with a* 250 nm *coupling distance.*

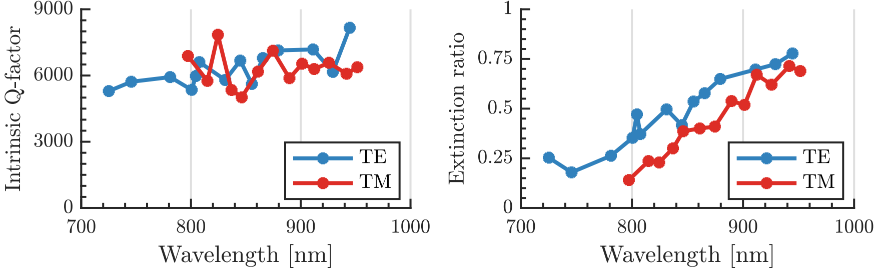

Figure 4.6: *Loaded Q-value and extinction ratio trends for an all-pass PMN-PT single ring resonator with coupling gap of* 200 nm.

Figure 4.6 shows the loaded Q-value and extinction ratio trends for the 200 nm coupling gap all-pass resonator. The extinction ratio trend corresponds well with the theoretical prediction, but the (almost) absent trend in the Q-factor reveal that the wavelength dependent quality factor due to the coupling constant is negligible to the component related to propagation loss and cavity quality. This is confirmed by the fact that the here absent trend is present within the higher quality (lower loss) silicon substrate devices.

The experimentally extracted group delay for the all-pass resonators were on the order of 15 ps to 30 ps which is well below the delays predicted, much owing to the large propagation losses of the devices.

Moving on, the 5-ring CROW spectral response is shown in figures 4.7 and 4.8 for the drop and through ports respectively. These display the expected behaviour and reveal approximately nanometre wide resonances taking the shape of five convoluted single ring resonances with experimentally extracted drop port delays of around 90 ps.

In the transmission spectroscopy spectra, the full convoluted resonance shape is hard to distinguish for several reasons. Firstly, the fact that the intrinsic quality factors are low due to waveguide loss implies that the resonator ring couplings are not strong enough to the produce mode-splitting required to see the full spectral profile. Secondly, the different spectral components of the spectra are hypersensitive to polarisation filtering and location within the beam spot itself causing

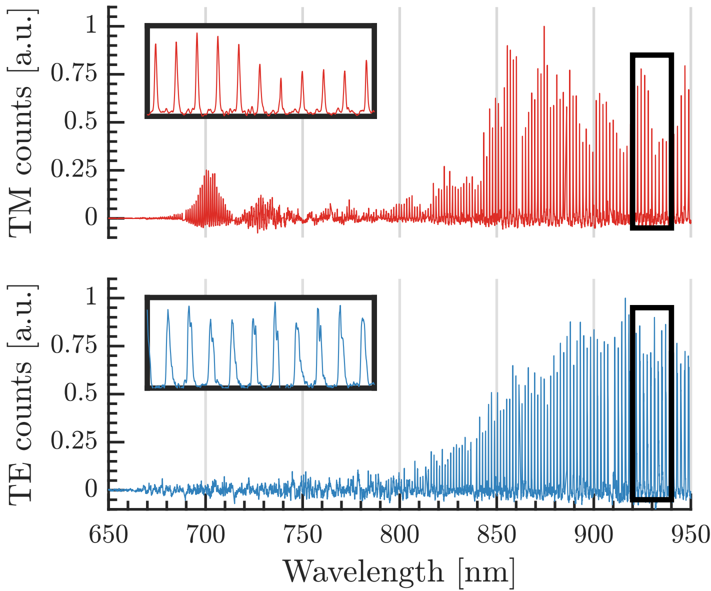

Figure 4.7: *Flattened TE and TM spectral response for a 5-ring CROW on a PMN-PT substrate for the drop port.*

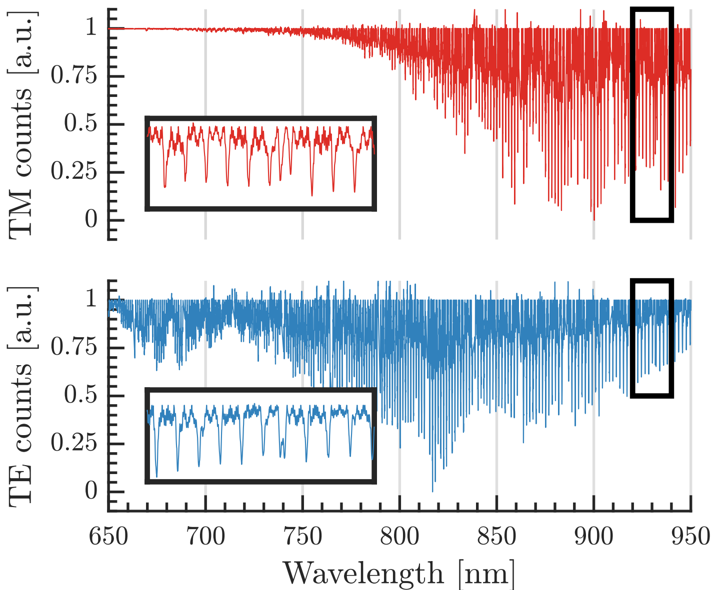

Figure 4.8: *Flattened TE and TM spectral response for a 5-ring CROW on a PMN-PT substrate for the through port.*

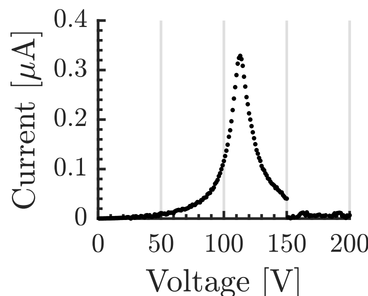

Figure 4.9: *IV poling curve for the PMN-PT substrate.*

some components to take precedent over others. Altogether, these effects effectively smear out the individual component's spatial features resulting in single resonances instead of the clean convoluted lineshape theoretically predicted.

Moving on to the piezoelectric tuning of the resonances, the 5-ring CROW and two ring resonators were tuned piezoelectrically. Prior to this, the sample was electrically poled, the results of which are shown in figure 4.9. This was done in order to align the electrical domains of the PMN-PT to further enhance the tuning strength and also to gauge the piezoelectric performance of the substrate in question. As the poling IV-curve reveal, the domains aligned at ≈110 V and currents on the order of µA was achieved. The poling process was carried out as close to adiabatically as possible, meaning that the voltage shifts were kept to one volt steps at maximum, and that the setting time for each transition was long enough to prevent any sudden voltage changes, which could cause the substrate to shatter.

In determining the poling conditions and rate, previous knowledge of the behaviour and domain switching voltages for samples of the same type as well the substrate thickness was taken into account. The poling was performed with the assistance of Thomas Lettner.

Following the poling, voltage dependent transmission spectroscopy measurements were taken, meaning that a spectrum was collected for each voltage setting (going from 0 V to 200 V in 1 V steps). The feature of interest in this measurement is not the spectra directly, but rather the tuning effect the voltage shift has. Therefore, a Lorentzian lineshape was fitted to a selected resonance for each step, and by

tracing the fitted lineshape resonance wavelength, the resonance shift as a function of the applied voltage could be collected.

For the two single ring resonators, the wavelength tuning is shown in figure 4.10 which show an approximate 0.12 nm shift for the maximum applied voltage. However, the same strain could be applied but in the reversed direction by applying the same negative voltage (i.e. if positive voltage stretches the piezoelectric substrate along the bi-axial surface the devices are patterned on, the same negative voltage would compress the sample). Therefore, the tuning range for the single rings is approximately ± 0.12 nm, or equivalently, 0.24 nm.

The piezoelectric tuning of the 5-ring CROW is shown in figure 4.11 for the through and drop ports respectively. There, shifts of between 0.10 nm and 0.15 nm are shown depending on which port and polarisation one looks at. Therefore, the tuning range, which is twice the range of the shifts in the positive direction, is between 0.20 nm and 0.30 nm, again depending on the port and polarisation. This tuning range translates to a 90 ps group delay tuning (moving from 90 ps on resonance at 0 V to 0 ps 0.3 nm off resonance at 200 V).

Here, a positive voltage induced a blueshift to the resonance while negative voltage would conversely redshift the resonances. Figures 4.12 and 4.13 shows the blueshifted spectra of the two tuning extrema at 0 V and 200 V once again highlighting the tuning range of the fabricated devices.

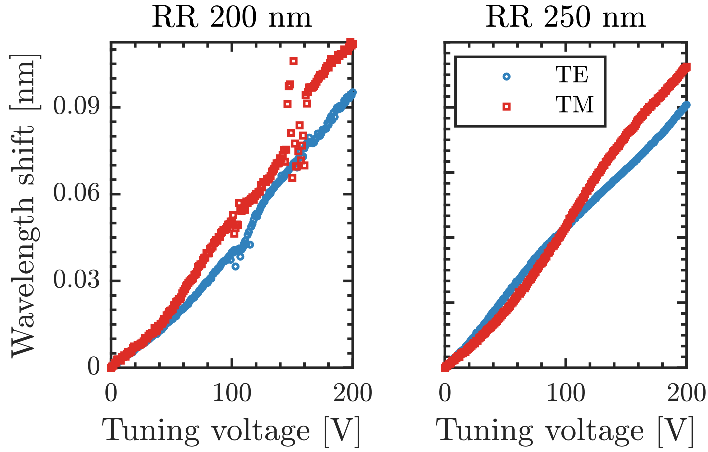

Figure 4.10: *Resonance shift as a function of the tuning wavelength for the two single ring resonators with* 200 nm *(left) and* 250 nm *(right) coupling distances respectively for the TE and TM modes.*

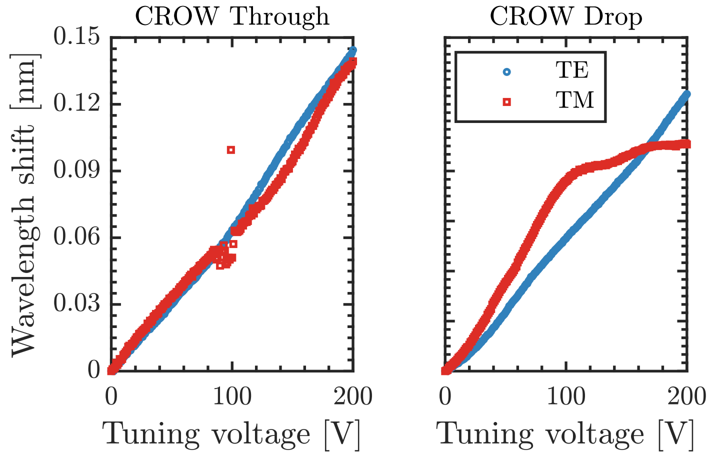

Figure 4.11: *Resonance shift as a function of the tuning wavelength for the 5-ring CROW through (left) and drop (left) ports respectively, for the TE and TM modes.*

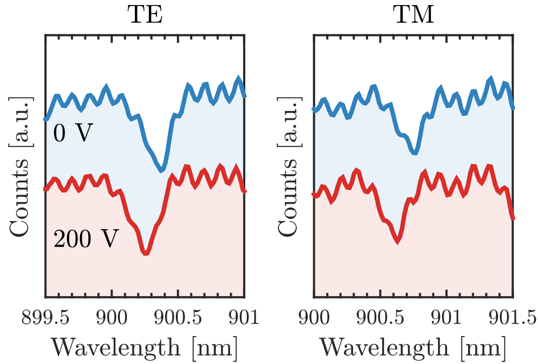

Figure 4.12: *Spectra for the two tuning extrema at* 0 V *(red) and* 200 V *(blue) showing the spectral shift for the TE and TM modes in a* 200 nm *gap ring resonator.*

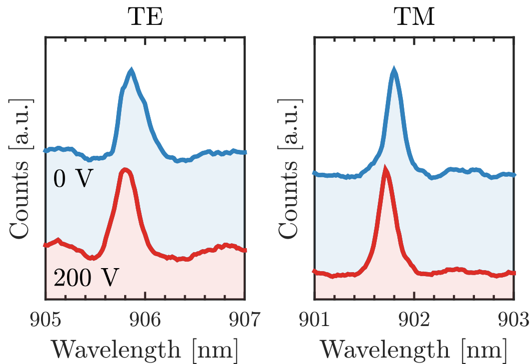

Figure 4.13: *Spectra for the two tuning extrema at* 0 V *(red) and* 200 V *(blue) showing the spectral shift for the TE and TM modes in a CROW drop port.*

5 | Discussion

The aim and objective of this thesis was to investigate, fabricate and characterise different quantum optical on-chip devices that could serve as possible delay line replacements. Furthermore, we set out to create an on-chip delay device that was tunable, while still keeping the requirements for device scalability, operating regimes and miniaturisation.

To achieve this, we firstly laid out the challenges and starting point in Chapter 1. We then presented the theoretical framework governing these types of devices and expanded on where and how these devices can provide efficient signal delays as well as providing a framework for numerical simulations, both in the spatial domain and in the time domain. Furthermore, we showed some results from these numerical tools, specifically highlighting the spectral characteristics of all-pass ring resonators, add-drop resonators as well as for the more general CROW resonator.

One of the main characteristics of these resonators is the coupling and transmission strengths, which in principle depend on the coupling distance (i.e. the distance over which the evanescent field coupling takes place). Therefore, we also provided numerical FDTD 2.5D simulations for this in Chapter 2 which showed intensity coupling fractions between roughly 0.75 and 0 for coupler gaps of 50 nm to 400 nm. Noticeably, the TM mode yield stronger coupling parameters than the TE mode in both the straight bus-ring resonator and bent bus-ring resonator setups as expected, which is due to the stronger mode delocalisation in the bent waveguides (and therefore by extension in the ring resonators).

Then, a practical prototyping phase commenced, where we fabri-

cated test designs of various elements on silicon substrates followed by an all-optical characterisation from which the fabrication recipes and process could be evaluated. After several iterations, the recipes and process presented in Chapter 3 were settled on. One of the primary considerations in increasing the cavity quality was the surface roughness of the devices, which was affected mainly by the etching in our fabrication process. Therefore, we experimented with helium backside cooling in addition to the regular etching, which is known for reducing the final surface roughness at the (severe) cost of creating sloped sidewalls.

In the prototyping, this was quickly ruled out as a viable fabrication strategy just due to the side-effect of sloped sidewalls, which caused the modal formation of the waveguides to go from single-mode to pseudo-multi-mode with a height varying width.

Furthermore, the dosages used in the electron beam lithography was an important fabrication consideration as well, and to effectively counteract the effect this had on the final devices, matrices of devices was fabricated on the same chip where each batch of devices was exposed using an increased dose. This allowed for testing the same device geometry with different dosages effectively and led to the final dosage and parameters presented in Chapter 3.

5.1 Silicon prototype devices

We have presented results from an excerpt of the fabricated silicon prototype devices obtaining all-pass resonance widths as low as 0.06 nm with corresponding loaded quality factors of 15000 which correspond to intrinsic quality factors at least twice of that accounting for the bus waveguide coupling losses. Furthermore, for the add-drop resonators we saw resonances as small as 0.02 nm giving loaded Q-values of 45000, and accounting for the two bus couplings this gives intrinsic Q-values in the 10^5 regime and (linear) propagation losses around 1 dB/cm.

These figures were then used for developing a CROW design that numerically was capable of creating delays above 50 ps which is an arbitrary number but chosen to be able to experimentally extract the delay as the time jitter of the available equipment is on that order. A

number of different CROW designs were tested, but a 5-ring CROW with the same size rings as the single ring resonators was settled on as it theoretically put the delay in the correct regime, had sub-nanometre wide resonances (not wider than the FSR of the structure) while still not giving an overly complicated spectral response.

5.2 PMN-PT tunable devices

Two PMN-PT chips were used for developing the fabrication and pre-measurement procedures, and here we have only presented the latter of the two as the first chip encountered many mishaps which resulted in poor optical performance as well as poor tuning performance.

As mentioned earlier, the main goal of the piezoelectric substrate is to introduce the tuning to the already-designed devices. Therefore, the designs and recipes that gave the optimal all-optical performance were chosen for manufacturing. The all-optical measurements of the piezoelectric substrate revealed much broader resonances, which correspond to poorer quality cavities with loaded and intrinsic Q-values below 10000 compared to the order of magnitude higher result for the silicon prototyping. This indicate additional sources of loss in the form of for example scattering centre within the structures.

However, the main purpose of these substrates was to demonstrate tuning of the fabricated devices, not achieve the highest Q-factors, albeit this would have been desired as well. As we have shown, tuning ranges of up to 0.3 nm was achieved, which effectively mean that the device tolerances in fabrication can be mitigated. Grown, for example, QDs can present slight emission wavelength variations, which by this method can be mitigated.

Furthermore, the tuning shown in this thesis was conducted in room temperature, which increases the magnitude of the piezoelectric effect, but limit the magnitude of the applied voltage. One idea is to pole the sample and then cool it down to cryogenic temperatures while still holding the poling voltage. This effectively freezes the domains in place allowing for larger tuning spans but foremost also allows for extending the tuning range to the negative voltages without repoling the sample.

The PMN-PT chips also proved to be much more challenging to

fabricate devices on, much due to being more fragile than the pure silicon wafers. This led to an even higher degree of randomness in cleaving, and furthermore led to issues with the deposited thin-film gold contacts. For the prototyping PMN-PT chip (which was 200 µm thick, 2.5 times thinner than the real one), the gold film tore off underneath the deposited silicon nitride and oxide layers in the cleaving process. This was mitigated somewhat by cleaving the chip upside down, but for some degree of determinism we found that a thicker PMN-PT chip (500 µm) eliminated the issue completely.

5.3 Future work

This thesis and the work that has been put into it has laid a solid foundation for continuing the research aiming for novel designs and implementations of the proposed elements. The natural continuation of this work is to in addition to the transmission spectroscopy measurements, also take pure time-domain measurements where the time response to an input pulse can be determined (as in figure 2.14). This allows for a direct measurement of the circuit delay and with the results presented herein constitute an exhaustive investigation of the quantum delay circuits. Unfortunately, these measurements could not be conducted within the frame for this thesis due to time constraints.

Another aspect that would be interesting to look into, and the direction that the development is taking, is to individually tune single devices on a chip containing multiple devices. This goal is aligned with the future of utilising these delay lines in complex quantum computing schemes, but the practical implementation has some potential challenges. Firstly, the strain transfer and piezoelectric tuning needs to be deterministic and localised to the regions where delay devices are fabricated. Secondly, the electrical contacting becomes a much larger issue as the individual contacts needs to be contacted separately which not only requires individual cables on chip but also multi-channel/multiple voltage sources.

Finally, this project has run prior to and now alongside an implementation project that serves to combine single photon quantum dot emitters with the advanced tunable filtering structures developed in this theses. Figure 5.1 shows a preliminary second order corre-

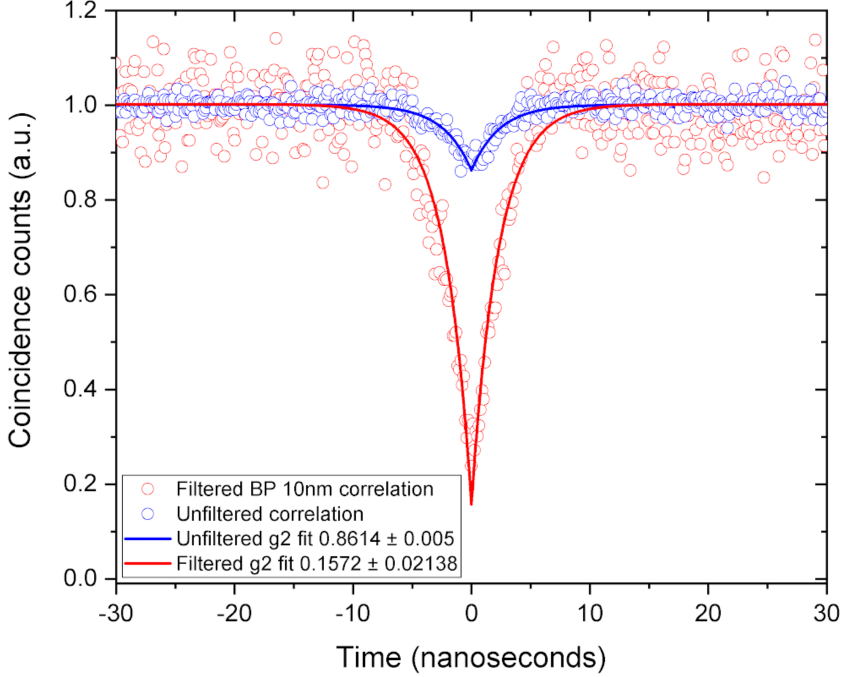

Figure 5.1: *Second order correlation measurement for a hBN quantum dot emitter without (blue) and with (red) spectral filtering. Courtesy of Ali Elshaari and Anas Skalli.*

lation measurement (courtesy of Ali Elshaari and Anas Skalli) for a hBN quantum emitter with (red) and without (blue) spectral filtering. Already without filtering the quantum dot emits single photons, but with spectral filtering (in this case achieved though spectrometer filtering) $g^{(2)} = 0.15$ are achieved.

The combination of these sources with the complex filtering structures developed here would greatly reduce the footprint of this type of circuits (moving from a $1\,\mathrm{m}^2$ spectrometer to a micrometer scale integrated chip) and allow for the envisioned type of complex multi-stage on-chip single photon emission and filtering (see for example [42]).

References

1. O'Brien, J. L., Furusawa, A. & Vučković, J. Photonic quantum technologies. *Nature Photonics* **3,** 687–695. `http://doi.org/10.1038/nphoton.2009.229` (2009).
2. Planck, M. K. E. L. Über eine Verbesserung der Wienschen Spectralgleichung. *Verhandl. Dtsc. Phys. Ges.* **2,** 202 (1900).
3. Clauser, J. F. Experimental distinction between the quantum and classical field-theoretic predictions for the photoelectric effect. *Physical Review D* **9,** 853–860. `http://doi.org/10.1103/PhysRevD.9.853` (1974).
4. Kimble, H. J., Dagenais, M. & Mandel, L. Photon Antibunching in Resonance Fluorescence. *Physical Review Letters* **39,** 691–695. `http://doi.org/10.1103/PhysRevLett.39.691` (1977).
5. Basché, T., Moerner, W. E., Orrit, M. & Talon, H. Photon antibunching in the fluorescence of a single dye molecule trapped in a solid. *Physical Review Letters* **69,** 1516–1519. `http://doi.org/10.1103/PhysRevLett.69.1516` (1992).
6. Kurtsiefer, C., Mayer, S., Zarda, P. & Weinfurter, H. Stable solid-state source of single photons. *Physical Review Letters* **85,** 290–293. `http://doi.org/10.1103/PhysRevLett.85.290` (2000).
7. Tran, T. T., Bray, K., Ford, M. J., Toth, M. & Aharonovich, I. Quantum emission from hexagonal boron nitride monolayers. *Nature Nanotechnology* **11,** 37–41. `http://doi.org/10.1038/nnano.2015.242` (2016).

8. Lohrmann, A. *et al.* Activation and control of visible single defects in 4H-, 6H-, and 3C-SiC by oxidation. *Applied Physics Letters* **108,** 021107. http://doi.org/10.1063/1.4939906 (2016).
9. Claudon, J. *et al.* A highly efficient single-photon source based on a quantum dot in a photonic nanowire. *Nature Photonics* **4,** 174–177. http://doi.org/10.1038/nphoton.2009.287 (2010).
10. Aharonovich, I., Englund, D. & Toth, M. Solid-state single-photon emitters. *Nature Photonics* **10,** 631–641. http://doi.org/10.1038/nphoton.2016.186 (2016).
11. Yoshizawa, A., Kaji, R. & Tsuchida, H. Generation of polarisation-entangled photon pairs at 1550 nm using two PPLN waveguides. *Electronics Letters* **39,** 621. http://doi.org/10.1049/el:20030400 (2003).
12. Akopian, N. *et al.* Entangled photon pairs from semiconductor quantum dots. *Physical Review Letters* **96.** http://doi.org/10.1103/PhysRevLett.96.130501 (2006).
13. Di Giuseppe, G. *et al.* Einstein-Podolsky-Rosen spatial entanglement in ordered and Anderson photonic lattices. *Physical Review Letters* **110,** 150503. http://doi.org/10.1103/PhysRevLett.110.150503 (2013).
14. Wang, J. *et al.* Multidimensional quantum entanglement with large-scale integrated optics. *Science* **360,** 285–291. http://doi.org/10.1126/science.aar7053 (2018).
15. Olislager, L. *et al.* Frequency-bin entangled photons. *Physical Review A - Atomic, Molecular, and Optical Physics* **82,** 013804. http://doi.org/10.1103/PhysRevA.82.013804 (2010).
16. Kobayashi, T. *et al.* Frequency-domain Hong-Ou-Mandel interference. *Nature Photonics* **10,** 441–444. http://doi.org/10.1038/nphoton.2016.74 (2016).
17. Marcikic, I. *et al.* Distribution of time-bin qubits over 50 km of optical fiber. *Physical Review Letters* **93,** 180502. http://doi.org/10.1103/PhysRevLett.93.180502 (2004).
18. Jayakumar, H. *et al.* Time-bin entangled photons from a quantum dot. *Nature Communications* **5,** 4251. http://doi.org/10.1038/ncomms5251 (2014).

19. Wakabayashi, R. *et al.* Time-bin entangled photon pair generation from Si micro-ring resonator. *Optics Express* **23,** 1103. http://doi.org/10.1364/oe.23.001103 (2015).
20. Barreiro, J. T., Langford, N. K., Peters, N. A. & Kwiat, P. G. Generation of hyperentangled photon pairs. *Physical Review Letters* **95,** 260501. http://doi.org/10.1103/PhysRevLett.95.260501 (2005).
21. Fickler, R. *et al.* Interface between path and orbital angular momentum entanglement for high-dimensional photonic quantum information. *Nature Communications* **5,** 4502. http://doi.org/10.1038/ncomms5502 (2014).
22. Prilmüller, M. *et al.* Hyperentanglement of Photons Emitted by a Quantum Dot. *Physical Review Letters* **121,** 110503. http://doi.org/10.1103/PhysRevLett.121.110503 (2018).
23. Knill, E., Laflamme, R. & Milburn, G. J. A scheme for efficient quantum computation with linear optics. *Nature* **409,** 46–52. http://doi.org/10.1038/35051009 (2001).
24. Grover, L. K. A fast quantum mechanical algorithm for database search. *Proceedings of the twenty-eighth annual ACM symposium on Theory of computing - STOC '96,* 212–219. http://doi.org/10.1145/237814.237866 (1996).
25. Shor, P. *Algorithms for quantum computation: discrete logarithms and factoring* in *Proceedings 35th Annual Symposium on Foundations of Computer Science* (IEEE Comput. Soc. Press, 2002), 124–134. http://doi.org/10.1109/sfcs.1994.365700.
26. Bernstein, D. J., Heninger, N., Lou, P. & Valenta, L. *Post-quantum RSA* in *Lecture Notes in Computer Science (including subseries Lecture Notes in Artificial Intelligence and Lecture Notes in Bioinformatics)* **10346 LNCS** (Springer, Cham, 2017), 311–329. http://doi.org/10.1007/978-3-319-59879-6{_}18.
27. Kok, P. *et al.* Linear optical quantum computing with photonic qubits. *Reviews of Modern Physics* **79,** 135–174. http://doi.org/10.1103/RevModPhys.79.135 (2007).

28. Zadeh, I. E. *et al.* Deterministic Integration of Single Photon Sources in Silicon Based Photonic Circuits. *Nano Letters* **16,** 2289–2294. http://doi.org/10.1021/acs.nanolett.5b04709 (2016).

29. Elshaari, A. W. *et al.* Strain-Tunable Quantum Integrated Photonics. *Nano Letters* **18,** 7969–7976. http://doi.org/10.1021/acs.nanolett.8b03937 (2018).

30. Somaschi, N. *et al.* Near-optimal single-photon sources in the solid state. *Nature Photonics* **10,** 340–345. http://doi.org/10.1038/nphoton.2016.23 (2016).

31. Senellart, P., Solomon, G. & White, A. High-performance semiconductor quantum-dot single-photon sources. *Nature Nanotechnology* **12,** 1026–1039. http://doi.org/10.1038/nnano.2017.218 (2017).

32. Schweickert, L. *et al.* On-demand generation of background-free single photons from a solid-state source. *Applied Physics Letters* **112,** 093106. http://doi.org/10.1063/1.5020038 (2018).

33. Badolato, A. *et al.* Deterministic coupling of single quantum dots to single nanocavity modes. *Science (New York, N.Y.)* **308,** 1158–61. http://doi.org/10.1126/science.1109815 (2005).

34. Reithmaier, G. *et al.* On-chip time resolved detection of quantum dot emission using integrated superconducting single photon detectors. *Scientific Reports* **3,** 1901. http://doi.org/10.1038/srep01901 (2013).

35. Reck, M., Zeilinger, A., Bernstein, H. J. & Bertani, P. Experimental realization of any discrete unitary operator. *Physical Review Letters* **73,** 58–61. http://doi.org/10.1103/PhysRevLett.73.58 (1994).

36. Martín-López, E. *et al.* Experimental realization of Shor's quantum factoring algorithm using qubit recycling. *Nature Photonics* **6,** 773–776. http://doi.org/10.1038/nphoton.2012.259 (2012).

37. Carolan, J. *et al.* Universal linear optics. *Science* **349,** 711–716. http://doi.org/10.1126/science.aab3642 (2015).

38. Gondarenko, A., Levy, J. S. & Lipson, M. High confinement micron-scale silicon nitride high Q ring resonator. *Optics Express* **17,** 11366. http://doi.org/10.1364/oe.17.011366 (2009).

39. Tien, M.-C., Bauters, J. F., Heck, M. J. R., Blumenthal, D. J. & Bowers, J. E. Ultra-low loss Si3N4 waveguides with low nonlinearity and high power handling capability. *Optics Express* **18,** 23562. http://doi.org/10.1364/oe.18.023562 (2010).

40. Bonneau, D., Silverstone, J. W. & Thompson, M. G. in *Topics in Applied Physics* 6, 41–82 (2016). http://doi.org/10.1007/978-3-642-10503-6{_}2.

41. Marsili, F. *et al.* Detecting single infrared photons with 93% system efficiency. *Nature Photonics* **7,** 210–214. http://doi.org/10.1038/nphoton.2013.13 (2013).

42. Elshaari, A. W. *et al.* On-chip single photon filtering and multiplexing in hybrid quantum photonic circuits. *Nature Communications* **8.** http://doi.org/10.1038/s41467-017-00486-8 (2017).

43. Gourgues, R. *et al.* Controlled integration of selected detectors and emitters in photonic integrated circuits. *Optics Express* **27,** 3710. http://doi.org/10.1364/OE.27.003710 (2018).

44. Najafi, F. *et al.* On-chip detection of non-classical light by scalable integration of single-photon detectors. *Nature Communications* **6,** 5873. http://doi.org/10.1038/ncomms6873 (2015).

45. Reed, G. T., Mashanovich, G., Gardes, F. Y. & Thomson, D. J. Silicon optical modulators. *Nature Photonics* **4,** 518–526. http://doi.org/10.1038/nphoton.2010.179 (2010).

46. Yariv, A. *Photonics: Optical Electronics in Modern Communications* (Oxford Univ., 2007).

47. Alexander, K. *et al.* Nanophotonic Pockels modulators on a silicon nitride platform. *Nature Communications* **9,** 3444. http://doi.org/10.1038/s41467-018-05846-6 (2018).

48. Ikeda, K., Saperstein, R. E., Alic, N. & Fainman, Y. Thermal and Kerr nonlinear properties of plasma-deposited silicon nitride/silicon dioxide waveguides. *Optics Express* **16,** 12987. http://doi.org/10.1364/oe.16.012987 (2008).

49. Krückel, C. J. *et al.* Linear and nonlinear characterization of low-stress high-confinement silicon-rich nitride waveguides: erratum. *Optics Express* **25,** 7443. `http://doi.org/10.1364/oe.25.007443` (2017).
50. Kittel, C. *Introduction to Solid State Physics* **12.** `http://doi.org/10.1021/ja01569a094` (2005).
51. Kamikawachi, R. C. *et al.* Determination of thermo-optic coefficient in liquids with fiber Bragg grating refractometer. *Optics Communications* **281,** 621–625. `http://doi.org/10.1016/j.optcom.2007.10.023` (2008).
52. Soref, R. & Bennett, B. Electrooptical effects in silicon. *IEEE Journal of Quantum Electronics* **23,** 123–129. `http://doi.org/10.1109/JQE.1987.1073206` (1987).
53. Xu, Q., Schmidt, B., Pradhan, S. & Lipson, M. Micrometre-scale silicon electro-optic modulator. *Nature* **435,** 325–327. `http://doi.org/10.1038/nature03569` (2005).
54. Elshaari, A. W. & Preble, S. F. 10 Gb/s broadband silicon electro-optic absorption modulator. *Optics Communications* **283,** 2829–2834. `http://doi.org/10.1016/j.optcom.2010.03.048` (2010).
55. Ding, F. *et al.* Tuning the exciton binding energies in single self-assembled InGaAs/GaAs quantum dots by piezoelectric-induced biaxial stress. *Physical Review Letters* **104,** 067405. `http://doi.org/10.1103/PhysRevLett.104.067405` (2010).
56. Kumar, S. *et al.* Strain-induced tuning of the emission wavelength of high quality GaAs/AlGaAs quantum dots in the spectral range of the 87Rb D 2 lines. *Applied Physics Letters* **99,** 161118. `http://doi.org/10.1063/1.3653804` (2011).
57. Trotta, R. *et al.* Nanomembrane quantum-light-emitting diodes integrated onto piezoelectric actuators. *Advanced Materials* **24,** 2668–2672. `http://doi.org/10.1002/adma.201200537` (2012).

58. Errando-Herranz, C., Edinger, P. & Gylfason, K. B. *Dynamic dispersion tuning of silicon photonic waveguides by microelectromechanical actuation* in *2017 Conference on Lasers and Electro-Optics (CLEO) : proceedings : San Jose, California, USA, May 2017* (IEEE, 2017), SW1N.3. `http://doi.org/10.1364/cleo{_}si.2017.sw1n.3`.

59. Chang, W. Y. *et al.* Patterned nano-domains in PMN-PT single crystals. *Acta Materialia* **143,** 166–173. `http://doi.org/10.1016/j.actamat.2017.10.016` (2018).

60. TRS Technologies. *Measured and Derived Elastic Compliance Constants and Elastic Stiffness Constants for TRS X2B* `http://www.trstechnologies.com/Portals/0/PDF/Measured_and_Derived_Full_Matrix_TRSX2B.pdf` (2019).

61. Kiat, J. M. *et al.* Monoclinic structure of unpoled morphotropic high piezoelectric PMN-PT and PZN-PT compounds. *Physical Review B - Condensed Matter and Materials Physics* **65,** 641061–641064. `http://doi.org/10.1103/PhysRevB.65.064106` (2002).

62. Yin, Z. W., Luo, H. S., Wang, P. C. & Su, G. S. Growth, characterization and properties of relaxor ferroelectric PMN-PT single crystals. *Ferroelectrics* **229,** 207–216. `http://doi.org/10.1080/00150199908224341` (1999).

63. Sun, E. & Cao, W. Relaxor-based ferroelectric single crystals: Growth, domain engineering, characterization and applications. *Progress in Materials Science* **65,** 124–210. `http://doi.org/10.1016/j.pmatsci.2014.03.006` (2014).

64. Park, S. E. & Shrout, T. R. Ultrahigh strain and piezoelectric behavior in relaxor based ferroelectric single crystals. *Journal of Applied Physics* **82,** 1804–1811. `http://doi.org/10.1063/1.365983` (1997).

65. Bellaiche, L. & Vanderbilt, D. Intrinsic piezoelectric response in perovskite alloys: PMN-PT versus PZT. *Physical Review Letters* **83,** 1347–1350. `http://doi.org/10.1103/PhysRevLett.83.1347` (1999).

66. Martín-Sánchez, J. *et al.* Strain-tuning of the optical properties of semiconductor nanomaterials by integration onto piezoelectric actuators. *Semiconductor Science and Technology* **33,** 013001. http://doi.org/10.1088/1361-6641/aa9b53 (2018).

67. Hecht, E. *Optics* 5 ed. (Pearson Education Ltd, 2017).

68. Wang, L. J., Kuzmich, A. & Dogariu, A. Gain-assisted superluminal light propagation. *Nature* **406,** 277–279. http://doi.org/10.1038/35018520 (2000).

69. Tucker, R., Ku, P. & Chang-Hasnain, C. Delay-bandwidth product and storage density in slow-light optical buffers. *Electronics Letters* **41,** 208. http://doi.org/10.1049/el:20057426 (2005).

70. Baba, T. Slow light in photonic crystals. *Nature Photonics* **2,** 465–473. http://doi.org/10.1038/nphoton.2008.146 (2008).

71. Fleischhauer, M., Imamoglu, A. & Marangos, J. P. Electromagnetically induced transparency: Optics in coherent media. *Reviews of Modern Physics* **77,** 633–673. http://doi.org/10.1103/RevModPhys.77.633 (2005).

72. Van der Wal, C. H. *et al.* Atomic memory for correlated photon states. *Science* **301,** 196–200. http://doi.org/10.1126/science.1085946 (2003).

73. Hau, L. V., Dutton, Z., Behroozi, C. H. & Harris, S. E. Light speed reduction to 17 metres per second in an ultracold atomic gas. *Nature* **397,** 594–598 (1999).

74. Liu, C., Dutton, Z., Behroozi, C. H. & Hau, L. V. Observation of coherent optical information storage in an atomic medium using halted light pulses. *Nature* **409,** 490–493. http://doi.org/10.1038/35054017 (2001).

75. Longdell, J. J., Fraval, E., Sellars, M. J. & Manson, N. B. Stopped light with storage times greater than one second using electromagnetically induced transparency in a solid. *Physical Review Letters* **95,** 063601. http://doi.org/10.1103/PhysRevLett.95.063601 (2005).

76. Vlasov, Y. A., O'Boyle, M., Hamann, H. F. & McNab, S. J. Active control of slow light on a chip with photonic crystal waveguides. *Nature* **438,** 65–69. http://doi.org/10.1038/nature04210 (2005).

77. Ginsberg, N. S., Garner, S. R. & Hau, L. V. Coherent control of optical information with matter wave dynamics. *Nature* **445,** 623–626. http://doi.org/10.1038/nature05493 (2007).

78. Elshaari, A. W., Aboketaf, A. & Preble, S. F. Controlled storage of light in silicon cavities. *Optics Express* **18,** 3014. http://doi.org/10.1364/oe.18.003014 (2010).

79. Smith, D. D., Chang, H., Fuller, K. A., Rosenberger, A. T. & Boyd, R. W. Coupled-resonator-induced transparency. *Physical Review A* **69,** 063804. http://doi.org/10.1103/PhysRevA.69.063804 (2004).

80. Kubo, S., Mori, D. & Baba, T. Low-group-velocity and low-dispersion slow light in photonic crystal waveguides. *Optics Letters* **32,** 2981. http://doi.org/10.1364/ol.32.002981 (2007).

81. Krauss, T. F. Slow light in photonic crystal waveguides. *Journal of Physics D: Applied Physics* **40,** 2666–2670. http://doi.org/10.1088/0022-3727/40/9/S07 (2007).

82. Errando-Herranz, C., Niklaus, F., Stemme, G. & Gylfason, K. B. Low-power microelectromechanically tunable silicon photonic ring resonator add-drop filter. *Optics Letters* **40,** 3556. http://doi.org/10.1364/ol.40.003556 (2015).

83. Errando-Herranz, C., Niklaus, F., Stemme, G. & Gylfason, K. B. *A MEMS tunable photonic ring resonator with small footprint and large free spectral range* in *2015 Transducers - 2015 18th International Conference on Solid-State Sensors, Actuators and Microsystems, TRANSDUCERS 2015* (2015), 1001–1004. http://doi.org/10.1109/TRANSDUCERS.2015.7181094.

84. Errando-Herranz, C., Niklaus, F., Stemme, G. & Gylfason, K. B. *A low-power MEMS tunable photonic ring resonator* in *MEMS 2015* (2015), 53–56.

85. Canciamilla, A. *et al.* Silicon coupled-ring resonator structures for slow light applications: Potential, impairments and ultimate limits. *Journal of Optics* **12,** 7. http://doi.org/10.1088/2040-8978/12/10/104008 (2010).

86. Poon, J. *et al.* Matrix analysis of microring coupled-resonator optical waveguides. *Optics Express* **12,** 90. http://doi.org/10.1364/opex.12.000090 (2004).

87. Poon, J. K., Zhu, L., DeRose, G. A. & Yariv, A. Transmission and group delay of microring coupled-resonator optical waveguides. *Optics Letters* **31,** 456. http://doi.org/10.1364/ol.31.000456 (2006).

88. Poon, J. K. S., Scheuer, J., Xu, Y. & Yariv, A. Designing coupled-resonator optical waveguide delay lines. *Journal of the Optical Society of America B* **21,** 1665. http://doi.org/10.1364/josab.21.001665 (2004).

89. Xu, Q. *Controlling the flow of light on chip with microring resonators* PhD thesis (Cornell University, 2007).

90. Schwelb, O. Transmission, group delay, and dispersion in single-ring optical resonators and add/drop filters - A tutorial overview. *Journal of Lightwave Technology* **22,** 1380–1394. http://doi.org/10.1109/JLT.2004.827666 (2004).

91. Bogaerts, W. *et al.* Silicon microring resonators. *Laser and Photonics Reviews* **6,** 47–73. http://doi.org/10.1002/lpor.201100017 (2012).

92. Xu, D. X. *et al.* Extracting coupling and loss coefficients from a ring resonator. *Optics Express* **17,** 18971. http://doi.org/10.1364/oe.17.018971 (2009).

A Sample mounting

As discussed in the characterisation chapter (section 3.4), the piezoelectric samples need to be mounted in a manner that allows for electrical contacting on both the top and bottom gold contacts.

Figure A.1 shows the final mounting and contacting of the chip, while figure A.2 highlights the major components therein.

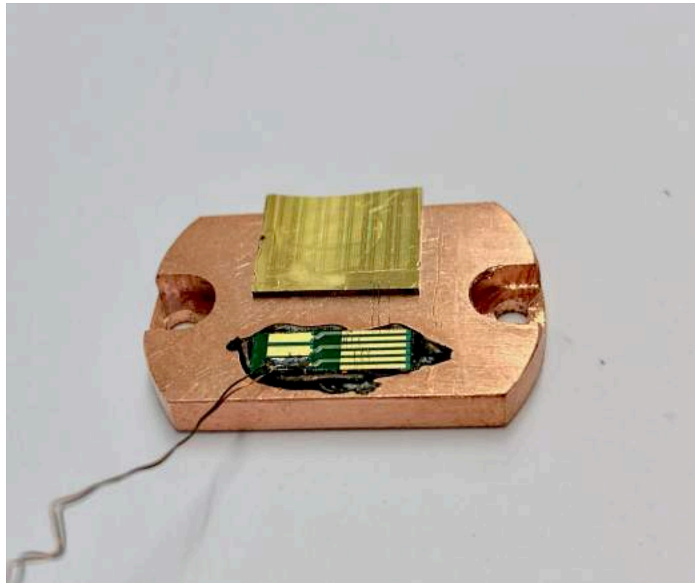

Figure A.1: *Overview of the finished sample mounted on the carrier copper plate.*

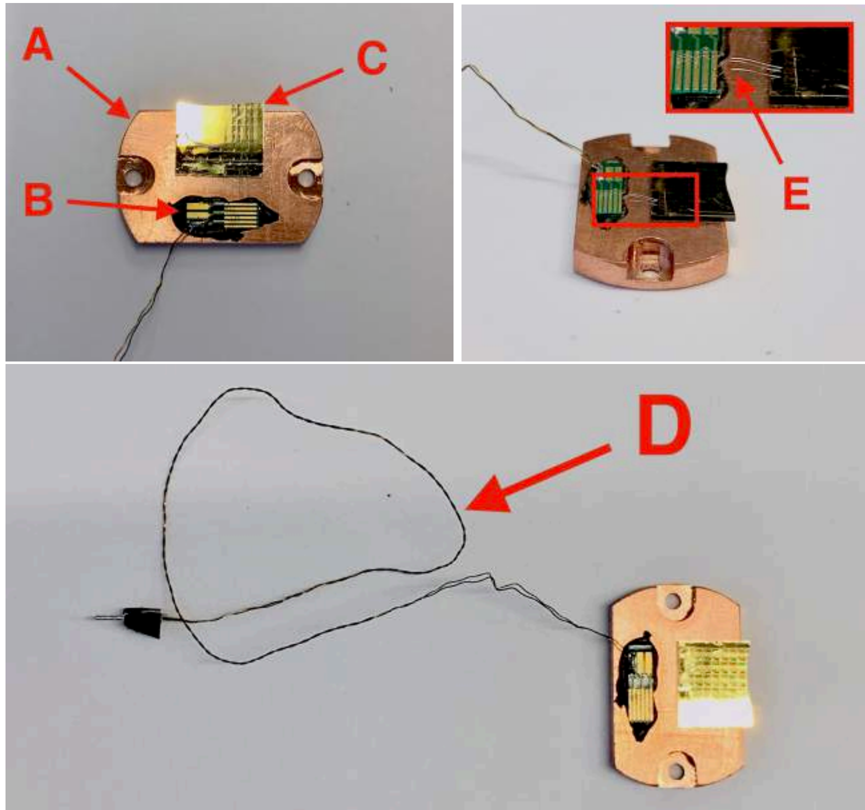

Figure A.2: *Photographs of the piezoelectric mounting highlighting A: the copper mounting base contacting the bottom plate, B: the PCB used for contacting the top chip contact and external cable, C: the piezoelectric chip, D: the external cable contacting the top contact and finally, E: the microscale silver wires bridging the PCB and the top gold contact.*

B | Measurement mounting

For mounting the sample holder in the measurement setup, the intermediate holder shown in figure B.1 was used. To this holder, an electrical wire was connected to serve as the external exposure of the sample bottom gold contact through the copper sample holder.

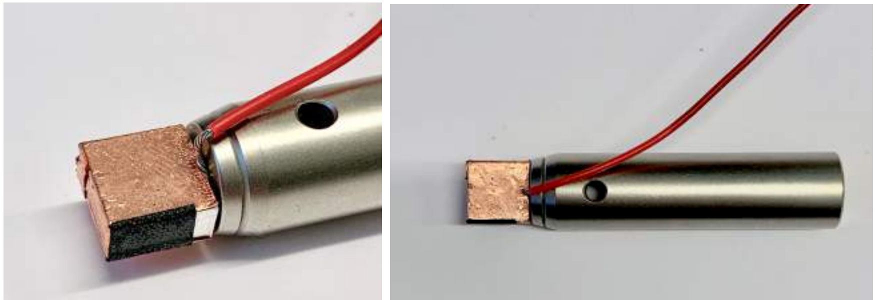

Figure B.1: *Intermediate mounting pole for the sample holder in the measurement setup with external wire.*

The sample holder with the piezoelectric chip was then attached to the intermediate pole by the adhesiveness of the mounting surface (figure B.1 left) in combination with a piece of copper tape to ensure the safety of the fabricated chip as well as to ensure stability throughout measurements as shown in figure B.2.

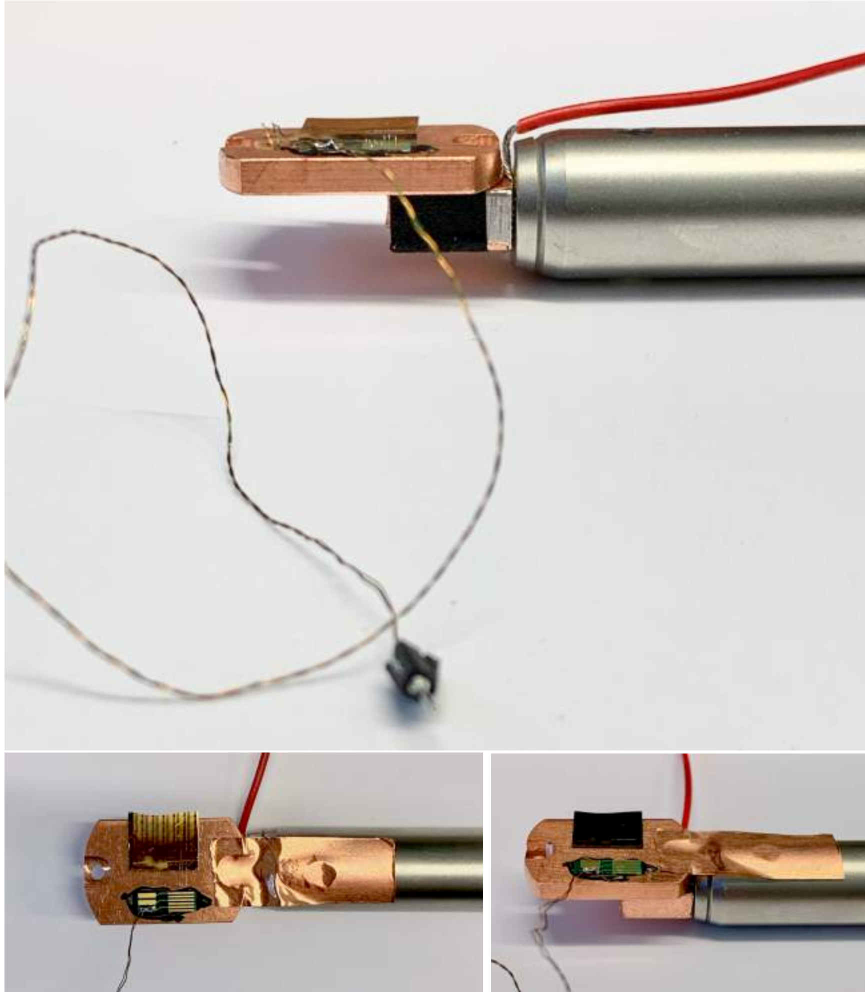

Figure B.2: *Final measurement mounting with copper tape applied for extra stability and security.*

C | Raw transmission spectroscopy spectra

Here we present the raw transmission spectroscopy spectra (the precursors) that was flattened into Figures 4.4, 4.5, 4.7 and 4.8.

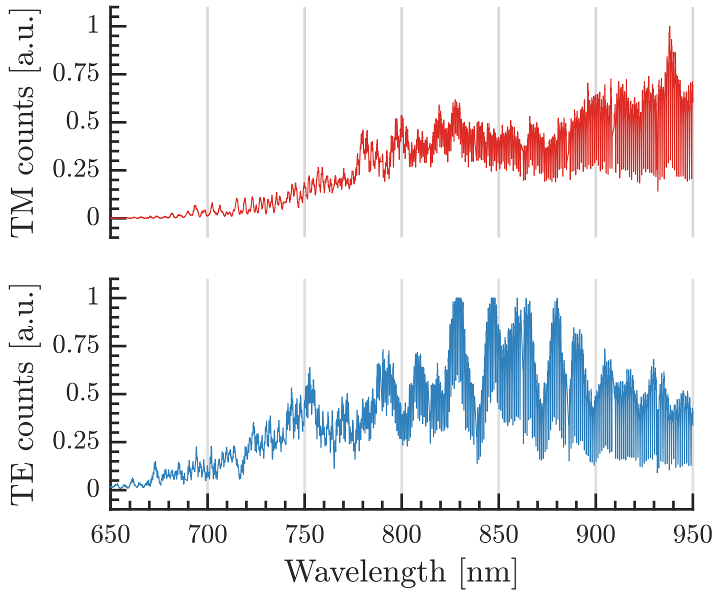

Figure C.1: *Raw TE and TM spectral response for a single ring resonator on a PMN-PT substrate with a* 200 nm *coupling distance.*

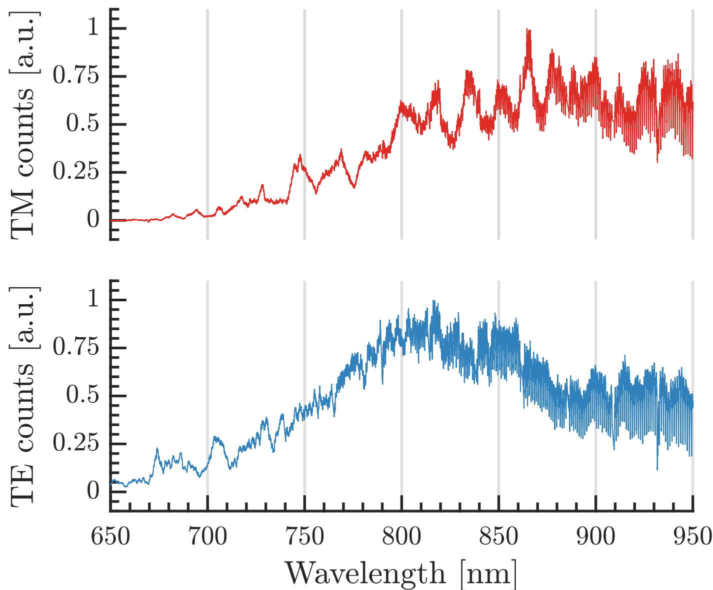

Figure C.2: *Raw TE and TM spectral response for a single ring resonator on a PMN-PT substrate with a* 250 nm *coupling distance.*

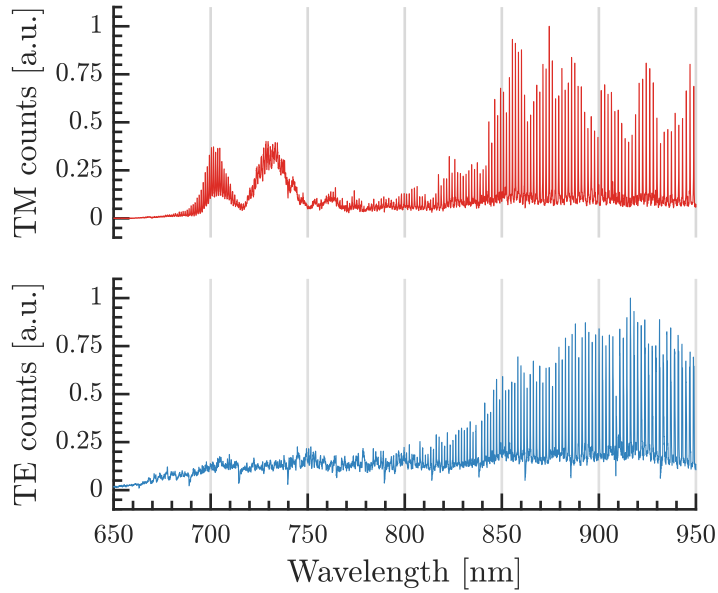

Figure C.3: *Raw TE and TM spectral response for a 5-ring CROW on a PMN-PT substrate for the drop port.*

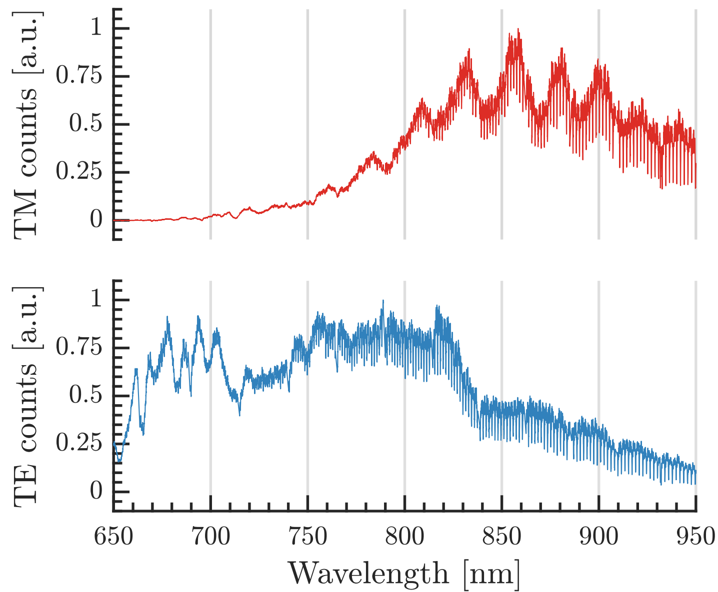

Figure C.4: *Raw TE and TM spectral response for a 5-ring CROW on a PMN-PT substrate for the through port.*

D Numerical models

Here, code snippets for the transfer matrix (listings D.1 through D.3) and time domain models (listing D.4 and D.5) will be presented.

Listing D.1: *Transfer Matrix: All-Pass*

```
% ============================================
% ====== Written by Anton Moller, 2019 =======
% ============================================

% Transmission spectra and group delay
% for an all-pass single ring resonator following
% the theory laid out in the thesis (eq 2.12/13/14)
clear all; close all;

% Initial coupling constants for calculating critical coupling
% and fix loss
%
% Coupling constants
kappa2 = 0.1^2;
t = sqrt(1-kappa2);

% Critical coupling gamma for kappa2 above
gamma = -log(t);

% Propagation attenuation, 40e-4 is the ring radius in cm
Alpha = gamma/(2*pi*40e-4); % [1/cm]

% Convert propatation loss to dB/cm
alpha = 10*log10(exp(-2*Alpha*1)); %[dB/cm]
loss = alpha;

% Phase vector
phi = linspace(-pi/4,pi/4,1000);

% Conversion from phi to physical units for
% group delay calculation.
%
% Roundtrip, effective index and angular frequency
```

```
34  L = 2*pi*(40e-6);
    Neff = 1.7;
36  w = phi.*(3e8)*Neff/L;

38  % Loop over varying coupling region constants
    % Critical coupling for tau = exp(-gamma)
40  % Overcoupled for tau < exp(-gamma)
    % Undercoupled for tau > exp(-gamma)
42  kappa_vector = [0.01, 0.05, 0.1, 0.15, 0.20];

44  for ii = 1:length(kappa_vector)

46      % Update coupling constants
        kappa2 = kappa_vector(ii)^2;
48      tau = sqrt(1-kappa2);

50      % Calculate the transmission amplitude A and
        % (power) transmission T following the theory
52      T_through = @(angle) 1 - (1-exp(-2*loss))*(1-tau^2)./ ...
            ((1-tau*exp(-loss))^2 + ...
54                              4.*tau^2.*exp(-loss).*sin(phi./2).^2);

56      A_through = @(angle) tau-(kappa2.*exp(-loss+i.*angle))./...
            ( 1- tau.*exp(-loss+i.*angle) );
58
        % Calculate the group delay by the derivative of the argument
60      % of the transmission amplitude following
        % https://ieeexplore.ieee.org/document/1298867
62      argS = angle(A_through(phi));
        delay = gradient(argS, (w(end)-w(end-1)));
64
        % Here, one can plot the result or save it...
66      % Transmission(phi) or TransmissionAmplitude(phi)
        % and the delay vs w.
68  end
```

Listing D.2: *Transfer Matrix: Add-Drop*

```
% ============================================
% ====== Written by Anton Moller, 2019 =======
% ============================================

% Transmission spectra and group delay
% for an add-drop single ring resonator following
% the theory laid out in the thesis (eq 2.21/22)
clear all; close all;

% Initial coupling constants for calculating critical coupling
% and fix loss
%
% Coupling constants
kappa2 = 0.1^2;
t = sqrt(1-kappa2);

% Critical coupling gamma for kappa2 above
gamma = -log(t);

% Propagation attenuation, 40e-4 is the ring radius in cm
Alpha = gamma/(2*pi*40e-4); % [1/cm]

% Convert propatation loss to dB/cm
alpha = 10*log10(exp(-2*Alpha*1)); %[dB/cm]
loss = alpha;

% Phase vector
phi = linspace(-pi/4,pi/4,1000);

% Conversion from phi to physical units for
% group delay calculation.
%
% Roundtrip, effective index and angular frequency
L = 2*pi*(40e-6);
Neff = 1.7;
w = phi.*(3e8)*Neff/L;

% Loop over varying coupling region constants
% Critical coupling for tau1 = tau2*exp(-gamma)
kappa_vector = [0.1, 0.2];

for ii = 1:length(kappa_vector)

    % Update coupling constants
    kappa2 = kappa_vector(ii)^2;
    tau = sqrt(1-kappa2);

    % Transmission amplitudes for drop and through ports
    A_through = @(angle) (tau-tau.*exp(-loss+i.*angle)) ...
                        ./( 1-tau^2.*exp(-loss+i.*angle) );
```

```
52      A_drop = @(angle) -(kappa2*exp(-loss/2 +i.*angle./2)) ...
                        ./( 1-tau^2.*exp(-loss+i.*angle) );
54
        % Calculate the group delay by the derivative of the argument
56      % of the transmission amplitude following
        % https://ieeexplore.ieee.org/document/1298867
58      delay_T = gradient(angle(A_through(phi)), (w(end)-w(end-1)));
        delay_D = gradient(angle(A_drop(phi)), (w(end)-w(end-1)));
60
        % Plot, save or process the results...
62  end
```

Listing D.3: *Transfer Matrix: CROW*

```
% ============================================
% ====== Written by Anton Moller, 2019 =======
% ============================================

% Transmission spectra and group delay
% for a CROW resonator following
% the theory laid out in the thesis (eq 2.35-39)
clear all; close all;

% Initial coupling constants for calculating critical coupling
% and fix loss
%
% Coupling constants
kappa2 = 0.1^2;
t = sqrt(1-kappa2);

% Critical coupling gamma for kappa2 above
gamma = -log(t);

% Propagation attenuation, 40e-4 is the ring radius in cm
Alpha = gamma/(2*pi*40e-4); % [1/cm]

% Convert propatation loss to dB/cm
alpha = 10*log10(exp(-2*Alpha*1)); %[dB/cm]
loss = alpha;
gam = alpha;

% Phase vector
phase = linspace(-pi/4,pi/4,1000);

% Number of coupling regions (#of rings = N-1)
N=5;

% Conversion from phi to physical units for
% group delay calculation.
%
% Roundtrip, effective index and angular frequency
L = 2*pi*(40e-6);
Neff = 1.7;
w = phi.*(3e8)*Neff/L;

% Coupling region constant for loop
kappa = 0.1;

% Through/Drop amplitudes allocation
ThroughA = zeros(1,length(phase));
DropA = zeros(1,length(phase));

% Coupling region transfer matrix components
t = [i/kappa, tau/(i*kappa); -tau/(i*kappa), -i/kappa ];
```

```
52 for k=1:length(phase)

54     % Update phase
       phi = phase(k);
56
       % Ring transfer matrix
58     Tj = t.*[exp(-gam/2 +i*phi/2), exp(-gam/2 +i*phi/2); ...
                   exp(gam/2 -i*phi/2), exp(gam/2 -i*phi/2) ];
60
       % System transfer matrix
62     T = Tj^N;

64     % System scattering matrix
       S = [T(1,1)-T(2,1)*T(1,2)/T(2,2), T(1,2)/T(2,2); ...
66                                   -T(2,1)/T(2,2), 1/T(2,2)];

68     % Drop and Through amplitude at phi
       DropA(k) = S(1,1);
70     ThroughA(k) = S(2,1);
   end
72
   % Physical (angular frequency) numerical step
74 step = w(end)-w(end-1);

76 % Calculate the group delay by the derivative of the argument
   % of the transmission amplitude following
78 % https://ieeexplore.ieee.org/document/1298867
   delay_T = gradient(angle(ThroughA), step);
80 delay_D = gradient(angle(DropA), step);
```

Listing D.4: *Time Domain: CROW*

```
% ============================================
% ====== Written by Anton Moller, 2019 =======
% ============================================
%
% Time domain model for a CROW resonator following
% the theory laid out in eq. 2.42-2.48
clear all; close all

% Speed of light
    c = 299792458;

% ============================================
% ============= CROW PARAMETERS ==============
% ============================================
%
% Number of coupling regions in CROW structure
% (#of rings = N-1)
    N = 10;

% Effective index and group index. Extracted from Lumerical
    neff = 1.7;
    ng = 2.28;

% Ring radius
    R=40E-6;

% Propagation loss [dB/cm]
    loss_per_cm=-1.7;

% Absorption cofficient [1/cm]
    Alpha = -loss_per_cm*log(10)/20;
% Coupling coefficients for each coupling region
    k=0.1.*ones(1,N);
    t=sqrt(1-k.^2);

% Resonance wavelengths for each ring
    desired_resonance_lambda = 900e-9;
    lambda_resonance = 2*pi*R*neff / ...
            floor(2*pi*R*neff/desired_resonance_lambda);

% The resonance detuning for each ring
    detuning = zeros(1,N);

% Vectorised resonance wavelengths
    lambda_res = detuning + lambda_resonance.*ones(1,N);

% Probe wavelength and corresponding detuned frequency
    lambda_probe = lambda_resonance + [-5:0.05:5].*1e-10;
    dw= c*2*pi*(1/lambda_resonance - 1./(lambda_probe));

% Physical round trip loss factors / phase accumulations
```

```
% R expressed in cm as Alpha is in 1/cm
    gamma_ring=Alpha*2*pi*(R*100);
    phase_ring=neff*(2*pi./lambda_res)*2*pi*R;


% ============================================
% ========== SIMULATION PARAMETERS ===========
% ============================================
%
% Simulation timesteps. Must be at least N*dt*4
    timesteps = 5000;

% Simulation timestep = time to propagate half a ring
    dt= (ng*pi*R/c);

% Electrical fields with dimensions for
% (time, interaction region, input detuning)
    Ea = zeros(timesteps, N, length(lambda_probe));
    Eb = zeros(timesteps, N, length(lambda_probe));
    Ec = zeros(timesteps, N, length(lambda_probe));
    Ed = zeros(timesteps, N, length(lambda_probe));
    time = zeros(timesteps,1);

% ============================================
% =============== SIMULATION =================
% ============================================
%
% Start at tt = 5 to allow for (tt-1) expressions as
% E evolve from injection in Ea(tt, m=1)
for tt=5:timesteps
    time(tt)=dt*tt;

    % Injection of gaussian pulse at input at time
    % t = 1000 ps with 50 ps width
    Ea(tt,1,:) = exp(-(time(tt)-1000E-12)^2/(50E-12)^2) ...
                        .*exp(1i*dw*time(tt));


    for m=1:N-1
        % Intra-ring dynamics
        Ed(tt,m,:) = Eb(tt-1,m+1,:).* ...
                    exp(-gamma_ring/2 + 1i*phase_ring(m)/2);
        Ea(tt,m+1,:) = Ec(tt-1,m,:).* ...
                    exp(-gamma_ring/2 + 1i*phase_ring(m)/2);

        % Coupling region dynamics
        Eb(tt,m,:) = t(m).*Ea(tt,m,:) + 1i*k(m).*Ed(tt,m,:);
        Ec(tt,m,:) = 1i*k(m).*Ea(tt,m,:) + t(m).*Ed(tt,m,:);
    end

    % Final exit region dynamics
    Eb(tt,N,:) = t(N).*Ea(tt,N,:);
    Ec(tt,N,:) = 1i*k(N).*Ea(tt,N,:);
```

```
106 end

108 % ==========================================
    % ============ RESULT EXTRACTION ============
110 % ==========================================
    %
112 % Squeeze E(time dimension, input detuning) to
    % remove the coupling region dimension and
114 % also square the electric field to get power
    P_in = squeeze(Ea(:,1,:).*conj(Ea(:,1,:)));
116 P_through = squeeze(Eb(:,1,:).*conj(Eb(:,1,:)));
    P_drop = squeeze(Ec(:,N,:).*conj(Ec(:,N,:)));
118
    % Normalise each field w.r.t. itself
120 for i=1:length(dw)
        P_in(:,i) = P_in(:,i)./max(P_in(:,i));
122     P_drop(:,i) = P_drop(:,i)./max(P_drop(:,i));
        P_through(:,i) = P_through(:,i)./max(P_through(:,i));
124 end

126 % Allocate and extract the delay from each detuning
    Delay = zeros(length(dw),1);
128 for index=1:length(dw)
        Delay(index) = abs(DelayCalculation(...
130                         P_in(:,index), P_drop(:,index), time));
    end
132
    % Extract maximum delay and save corresponding fields
134 [Y,I] = max(Delay);
    P = [P_in(:,I), P_through(:,I), P_drop(:,I)];
136
    % Save, plot or process result
```

Listing D.5: *Time Domain: CROW delay calculation function*

```
   function [delay] = DelayCalculation(input, trans, time)
 2 % DelayCalculation calculates the delay between the pulses
   % in the input timeseries and the transmission timeseries
 4 % by comparing the pulse maximum. Input and Trans must
   % share the same time parametrisation time.
 6 %
   % Returns the delay or 0 (with warning) if no maxima can
 8 % be found for the transmission series.
   %
10 % input - input timeseries
   % trans - transmission timeseries
12 % time  - time parametrisation

14     [~, inputMaxIndex] = max(input);
       [transMax, transMaxIndex] = max(trans);
16
```

```
18     if abs(transMax - min(trans)) < 1e-2
           delay = 0;
20         warning(['Delay: No maximum could be found in this' ...
               'iteration as the transmission timeseries' ...
22             ' is too flat'])
       else
24         delay = time(inputMaxIndex)-time(transMaxIndex);
       end
26 
   end
```